



POZNAŃ UNIVERSITY OF TECHNOLOGY

DOCTORAL THESIS

Direct approach noise analysis of a transonic axial compressor blade

Author:

MSc. Eng. Jędrzej MOSIEŻNY

Supervisor:

Prof. DSc. Eng. Michał CIAŁKOWSKI

*A thesis submitted in fulfilment of the requirements
for the degree of Doctor of Philosophy. Engineer.*

in the

Faculty of Work Machines and Transportation
Chair of Thermal Engineering

October 21, 2018

Declaration of Authorship

I, MSc. Eng. Jędrzej MOSIEŻNY, declare that this thesis titled, 'Direct approach noise analysis of a transonic axial compressor blade' and the work presented in it are my own. I confirm that:

- This work was done wholly or mainly while in candidature for a research degree at this University.
- Where any part of this thesis has previously been submitted for a degree or any other qualification at this University or any other institution, this has been clearly stated.
- Where I have consulted the published work of others, this is always clearly attributed.
- Where I have quoted from the work of others, the source is always given. With the exception of such quotations, this thesis is entirely my own work.
- I have acknowledged all main sources of help.
- Where the thesis is based on work done by myself jointly with others, I have made clear exactly what was done by others and what I have contributed myself.

Signed:

Date:

Abstract

This thesis proposes a method of assessing flow generated noise in transonic flows by direct formulation.

First a steady state Reynolds Averaged Navier-Stokes analysis of NASA R67 transonic axial compressor is performed as a validation study of the mesh and numerical setup. The result of the steady state analysis is then used as an initialization for transient DDES analysis performed on high quality, 11 million cells hexagonal mesh. The transient analysis covers 0.05s of physical flow time, which corresponds to about 800 revolutions of the rotor. Both steady state and transient simulations are performed on PL-Grid HPC infrastructure.

Transient results are analyzed with an in-house build program. The program uses information about static pressure, transient particle velocity and vorticity from each timestep. This data is then postprocessed into sound pressure levels, sound frequency and effective sound power level.

Information on generation of sound phenomena occurring in the blade passage are gathered from direct formulation and may be used as a validation case for FW-H or other computational aeroacoustic analogies dealing with flows in transonic regimes in rotating machinery.

Acknowledgements

In this place I would like to thank the Chair of Thermal Engineering of Poznań University of Technology, with special recognition to MSc. Eng. Bartosz Ziegler and PhD Eng. Przemysław Grzymisławski for thorough scientific and personal support during this project.

A big recognition goes to the owners and maintainers of the PLGRID - Polish HPC infrastructure, especially team in HPC Cyfronet center in AGH University of Science and Technology in Kraków. Being able to use the state of the art HPC clusters for analyses made this project possible.

Contents

Declaration of Authorship	iii
Abstract	v
Acknowledgements	vii
Contents	ix
List of Figures	xi
List of Tables	xiii
Abbreviations	xv
Symbols	xvii
Indices	xix
1 Introduction	1
1.1 Introduction and motivation	1
1.2 Growth of air traffic movements in early 20th century	2
1.2.1 Years 2000 – 2010	3
1.2.2 Years 2010 – 2035	4
1.3 Some excerpts from airworthiness regulations	6
1.3.1 CAEP regulations	8
1.3.2 ICAO Annex 16	8
1.3.3 Local regulations	10
1.4 Aircraft propulsion noise generation	13
2 Current research on Computational Aeroacoustics	17
2.1 Classification of CAA methods	17
2.2 Lighthill-Curle theory of aerodynamic sound	18
2.3 FW-H Analogy	20
2.4 Limitations to acoustic analogies	23
3 Approach and direct formulation of noise analysis	25
3.1 Direct formulation of noise analysis	25
3.2 CFD analysis requirements	27
3.2.1 Governing equations	28

3.2.2	Direct Numerical Simulation	28
3.2.3	Large Eddy Simulation	29
3.2.4	Reynolds Averaged Navier Stokes	32
3.2.5	Hybrid RANS/LES Methods	34
3.3	Mesh sizing requirements	36
3.4	Timestep requirements	39
3.5	Limiting factors of the direct approach	40
4	Test case	41
4.1	NASA Rotor 67 transonic axial compressor	41
4.2	3D geometry preparation	42
4.3	Meshing approach	43
5	CFD Analysis	49
5.1	Case preprocessing	49
5.2	Flowfield initialization & RANS	50
5.3	DDES analysis	52
5.4	Validation of the results	54
6	Results of flow field noise analysis	57
6.1	Transition from flow-field to sound signal data	57
6.2	Sound levels results	57
6.2.1	Results postprocessing	57
6.2.2	Qualitative analysis	58
6.2.3	Quantitative analysis	59
6.3	Frequency analysis results	60
6.3.1	Results postprocessing	60
6.3.2	Qualitative analysis	62
6.3.3	Quantitative analysis	63
7	Conclusions & Further work	65
7.1	Results discussion	65
7.2	Improvements to the method	66
7.3	Further work	67
7.4	Closing remarks	68
Bibliography		69

List of Figures

1.1	Number of aircraft registered in the EU (EUROSTAT)	3
1.2	Growth rate of number of aircraft registered in the EU	3
1.3	Total number of passengers in the EU (EUROSTAT)	4
1.4	Growth rate. Total number of passengers in the EU	4
1.5	Number of airports (EUROSTAT)	5
1.6	Growth rate. Number of airports (self study)	5
1.7	Average annual growth (scenario C: Regulated Growth) [2]	7
1.8	Total traffic in 2035 [2]	7
1.9	CDA approach (solid line) vs. Standard approach (dash line)	11
1.10	Heathrow noise contours. 83% western & 17% eastern traffic [18]	12
1.11	Sources of noise of a turbofan engine [28]	14
1.12	Impact of aircraft noise sources at take-off and landing [28]	14
1.13	Engine nacelle chevron on a GEnx engine	15
1.14	Exemplary anelysis on a chevron engine outlet [16]	15
3.1	Resolving eddies in different kinds of CFD analyses	28
3.2	Scenario 1. Wavelength smaller than cell edge length	37
3.3	Scenario 2. Wavelength equal to cell edge length	38
3.4	Scenario 3. Wavelength equal four minimum edge lengths	38
3.5	Scenario 4. Wavelength larger than four minimum edge lengths	38
4.1	Geometry of NASA R67	41
4.2	Final single passage geometry. Some features hidden for clarity	44
4.3	Mesh topology with conforming periodic boundaries	45
4.4	Mesh h-topology	45
4.5	Mesh quality histogram	47
4.6	Completed Mesh	47
5.1	Flowchart of the PISO algorithm	52
5.2	Constant pitch (left) and constant chord (right) lines [27]	54
5.3	Inlet pressure validation	55
5.4	Outlet pressure validation	55
6.1	Tip gap streamlines. Velocity in [m/s]	59
6.2	SPL to flowfield turbulence values correlation	60
6.3	SPL to flowfield turbulence values correlation	60
6.4	Exemplary FFT heatmap of magnitude. Random data.	61
6.5	SPL to flowfield turbulence values correlation	64
6.6	SPL to flowfield turbulence values correlation	64

List of Tables

1.1	Noise measurement points per ICAO Annex 16 [1]	10
1.2	Maximum noise levels per ICAO Annex 16 [1]	10
1.3	Noise Quota Count classification in Heathrow [18]	12
1.4	Examples of QC aircraft classification [18]	13
4.1	Basic R67 parameters	42
4.2	Test case boundary conditions	45
4.3	Location of compressor desing surfaces	46
5.1	Standard air properties	49
5.2	Test case boundary conditions	50

Abbreviations

APU	Auxillary Power Unit
BPF	Blade Passing Frequency
CAA	Computional Aero Acoustics
CAEP	Commitee on Aircraft Engine Emissions
CDA	Continuous Descent Approach
CFD	Computional Fluid Dynamics
CS	Coordinate System
DDES	Delayed Detached Eddy Simulation
DES	Detached Eddy Simulation
DFT	Discrete Fourier Transform
DNS	Direcr Numerical Situation
EPNdB	Effective Perceived Noise dB
FMG	Full Multi Grid
FVM	Finite Volume Method
FWH	Ffowcks Williams Hawkins
HPC	Hight Power Computing
HVAC	Heating Ventilation Air Conditioning
ICAO	International Civil Aviation Organization
IFR	Instrumental Flight Rrules
ILU	Incomplete Lower Upper
LDA	Laser Doppler Anemometry
LES	Large Eddy Simulation
MCA	Multiple Circular Approach
MTOW	Maximum Take Off Weight
N-S	Navier Stokes
PISO	Pressure Implicit with Splitting of Operators
RANS	Reynolds Averaged Nnavier Stokes
RMS	Root Mean Square
S-A	Spallart Allmaras
SAS	Scale Adaptive Simulation
SBES	Stress Blended Eddy Simulation
SDES	Shielded Detached Eddy Simulation
SGS	Sub Grid Scale
SPLdB	Sound Pressure Level dB
SILdB	Sound Intensity Level dB
SRS	Scale Rresolving Simulation
SST	Shear Stress Transport

Symbols

Amp	Amplitude	-
C_p	Specific heat at constant pressure	-
Co	Courant number	-
G	Filter function	-
M	Moll weight	-
Ma	Mach number	-
N	Total number of samples	-
$H(f)$	Heaviside function	-
P_i	Dipole acoustical strength	Pa
P_{ij}	Compression stress tensor	-
$Q(x, t)$	Mass introduced to system	kg
R	Gas constant	J/(kg · K)
Re	Reynolds number	-
S	Discontinuity surface	-
S_{ij}	Rate of Strain Tensor	-
T	Temeprature	K
T_{ij}	Lighthill stress tensor	-
U	Velocity vector	-
V	Integration volume	-
X	DFT complex coefficient	-
a	Speed of sound	m/s
d	Mesh wall spacing	m
e	Euler's number	-
f	Frequency	-
j	Imaginary number	-
k	k-th frequency bin	-
k	turbulence kinetic energy	-
n	Normal vector, n-th sample, number of blades, number of cells	-
p	Pressure	Pa
$q(t)$	Mass introduction rate	kg/s
r	Radiation vector	m
Δs	Mesh first layer thickness	m
t	Time	s
u, v, w	Velocity component	m/s
x, y, z	Distance over coordinate, location coordinate	m

Δ	Mesh wall spacing (Spalart-Allmaras)	m
Σ	Surface of discontinuity	-
δ	Mesh wall spacing (Spalart-Allmaras)	m
$\delta_{ij}, \delta(f)$	Dirac delta	-
η	Kolmogorov limit	-
θ	Phase shift	rad
κ	Polytropic index	-
λ	Wavelength	m
λ	Heat conductivity coefficient	W/(m · K)
ϕ	Conservation variable	-
ϕ'	Variable offset from average	-
$\bar{\phi}$	Filtered variable (LES derivation)	-
$\bar{\phi}$	Averaged variable (direct approach)	-
μ	Dynamic viscosity	Pa · s
μ_t	Turbulent viscosity	Pa · s
ν	Kinematic viscosity	m^2/s
$\tilde{\nu}$	Modified turbulent viscosity	m^2/s
ρ	Density	kg/m ³
σ_{ij}	Molecular viscosity stress tensor	-
τ	Retarded time	s
τ_{ij}	Subgrid scale tensor	s
ω	Angular frequency	rads ⁻¹
ω	Turbulence specific dissipation rate	-

Indices

0	initial, ambient conditions	-
<i>fric</i>	denotes friction component	-
<i>i, j</i>	summation indices	-
<i>k</i>	k-th sample, frequency bin	-
<i>n</i>	normal direction	-
<i>r</i>	radiation direction	-
<i>particle</i>	denotes particle specific value	-
<i>ref</i>	denotes reference value	-
<i>sound</i>	denotes sound value	-
<i>wall</i>	denotes near wall component	-
<i>wm</i>	wall modeled	-
<i>wr</i>	wall resolved	-
<i>x, y, z</i>	value in direction of coordinate	m

To my wife. For limitless patience. . .

Chapter 1

Introduction

1.1 Introduction and motivation

Pollution by sound conducted by aircraft becomes one of the major concerns while introducing new aircraft to the market. Airframe noise and engine noise are considered as disturbing to population inhabiting the areas near the aerodrome, especially during take-off and landing operations. The concerns regarding the influence of the aircraft noise on the surrounding environment lead to development of international regulations defining the limits of the Effective Perceived Noise Levels for aircraft of certain type or family, maximum take off weight and engine count, as well as methods for measuring the aircraft noise. Although relatively easy to conclude, measuring aircraft noise as described in the regulations in consideration is achievable only when the aircraft is capable of flying, which, obviously, is at the final end of the process of introducing the aircraft to the market.

In order to assess the noise of the aircraft a set of engineering methods allowing predicting the noise of the aircraft is conceived. Such methods include, but are not limited to, vibroacoustics describing the effect of vibrating elements of devices on generation of sound, and aeroacoustics describing the effect of airflow and flow with solid boundary interaction on generation of sound.

Aeroacoustics as such is a relatively new branch of physics combining the classical approach to propagation of sound with mathematical formulation of fluid flow known from fluid mechanics. It is said that modern approach to aeroacoustics originated with the works of Lighthill [19] [20] in mid 1950s. Combining the mathematical formulation of equations governing the fluid flow with equations describing wave propagation, sound power and sound intensity allowed to assess the sound levels of turbulent flow.

Along with improvements of the computational methods in fields of computational fluid dynamics, general numerical methods and availability of computational resources,

Computational Aero Acoustics (described further in this work as computational aeroacoustics) was developed as an engineering tool for assessing sound generated by fluid flow without the necessity of manufacturing the device and performing expensive experiments.

This thesis opens with a high level overview of commercial air traffic situation based on data provided by EUROSTAT. The development and changes in the IFR movements in the European Union airspace are presented along with the forecast prepared by EUROSTAT and EUROCONTROL. This is followed by a high level analysis of current requirements regarding the noise emissions of a non-military aircraft. Following is a brief study of components of an aircraft responsible for generating sound pollution during various stages of flight. It is established that one of the main sources of noise generated by the aircraft is the fan and first stage of the low pressure compressor and therefore this component shall be investigated further.

The main focus of this thesis is generation of sound by a single blade of a low pressure compressor. It is assumed, that identifying sources of noise in the compressor flow will provide an insight for designing an efficient compressor blade with reduced noise emission and, therefore, allow for designing a quieter jet engine which directly translates to a less noisy aircraft. A NASA R67 1st stage compressor blade is the test subject for the thesis. The given compressor was chosen as the operating parameters range is similar to a modern day first stage fan of a twin spool, large bypass turbofan engine and large quantities of experimental and validation data. A comparison between different aeroacoustic methods is provided and a modification to a direct noise analysis method is suggested. The blade for the compressor is than analyzed using the proposed method and results are visualized and presented. The work is concluded and suggestions for designing a compressor blade with reduced generation of noise are formulated, along with suggestions for further work within researching the generation of compressor noise.

1.2 Growth of air traffic movements in early 20th century

Statistical records on commercial air movement between countries in Europe since year 2000 is available from EUROSTAT. Information regarding number of passengers, flights, registered aircraft and number of airports in the 1st decade of 20th century is extracted to describe the increase in the movement of commercial aircraft. Furthermore, a brief analysis of the long term forecasts (up to year 2035) provide some predictions on the future air traffic. Both statistics of the past movements and long term forecasts show an increase in the commercial air traffic above Europe. Combining the increase of number of flight operations from existing airports with rapid urban sprawl leads to increasing noise pollution in the urban areas.

1.2.1 Years 2000 – 2010

First number to be shown is the total number of aircraft in the EU (fig. 1.1). Trends for passenger aircraft and total number of aircraft show a slow increase of these numbers. Chain growth ratio of number of aircraft (fig. 1.2) shows a rapid increase in year 2006 and stabilization afterwards. At this point situation on European skies is rather comforting. But comparing these numbers with figure 1.3 may change the perspective.

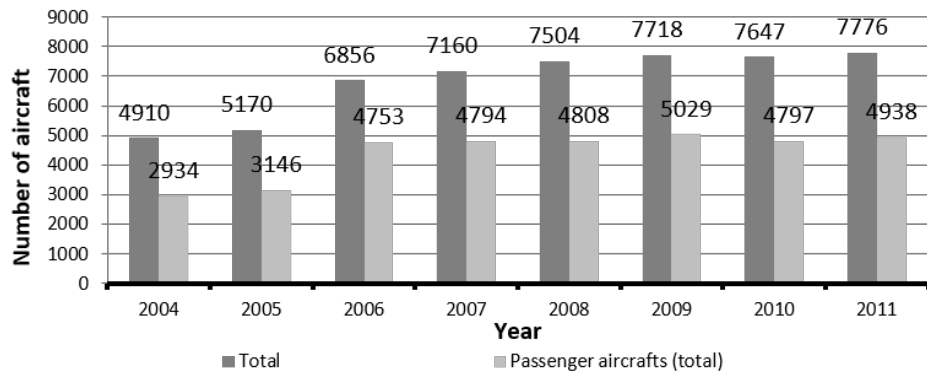


FIGURE 1.1: Number of aircraft registered in the EU (EUROSTAT)

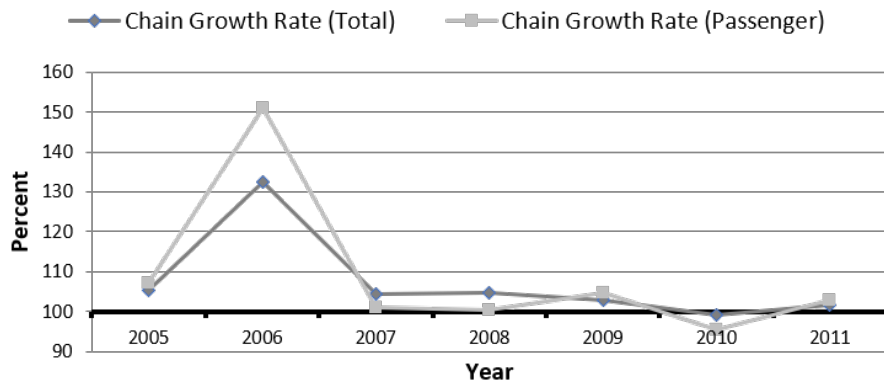


FIGURE 1.2: Growth rate of number of aircraft registered in the EU

As by figure 1.3, number of passengers is increasing, at average 50 to 70 million passengers every year. The growth rates (fig. 1.4) show large annual fluctuation of passenger count. Slowdown in year 2008 and decrease of passenger number in year 2009 are the aftermath of Financial Crisis of 2007-08. The situation recovers in years 2010-11. With roughly the same number of passenger airplanes (2007-11) this leads to rapid increase of passenger flights.

Existing fleet is supposed to deliver people and freight 24 hours a day, with very short overhaul periods, even shorter times to refuel and reload. Grounded aircraft generates loss instead of profit. Increasing number of flights generates yet another problem. All

airplanes need an airfield with proper infrastructure to perform flight operations, basic maintenance, serve passengers and so on.

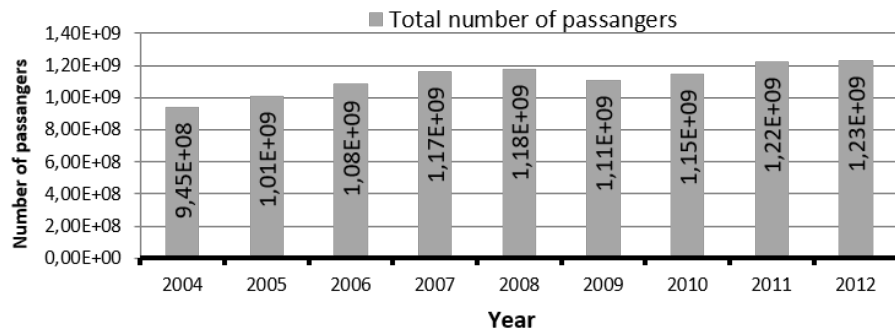


FIGURE 1.3: Total number of passengers in the EU (EUROSTAT)

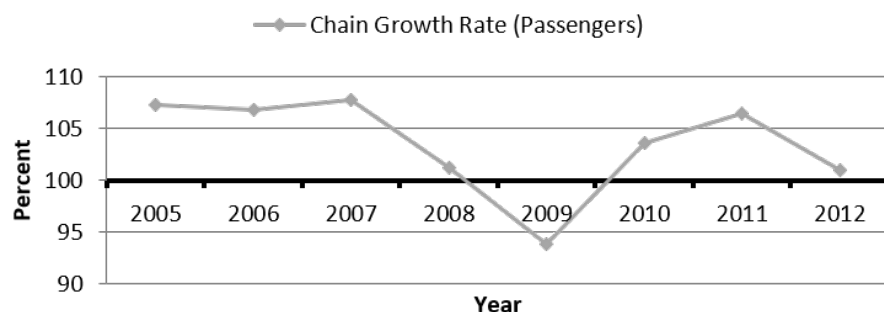


FIGURE 1.4: Growth rate. Total number of passengers in the EU

Surprisingly, the number of main airports is not following the trend set up by number of passengers. As seen on figure 1.5 number of main airports (serving more than 150 000 passengers a year) remains roughly the same, with very slight increase in research period. Change in number of main airports (fig. 1.6) is caused by varying number of passengers, rather than closing and opening airports. Decrease of number of airports in year 2009 is the aftermath of the economy crisis. Total number of airports varies among the years. This number includes small and medium airports such as club airfields and regional airports. Total number of airports (including registered regional and club airports) was under more influence of crisis and changed more rapidly.

1.2.2 Years 2010 – 2035

Trends presented in previous section may not give the full perspective. Years 2001–2012 show a significant increase in air traffic in Europe. Expansion of the EU in year 2004, Financial Crisis of 2007-2008, Arab Spring trampling through the Middle East and Northern Africa all have their reflection in air movements on the continent. These factors make the predictions harder than simple extrapolation of data.

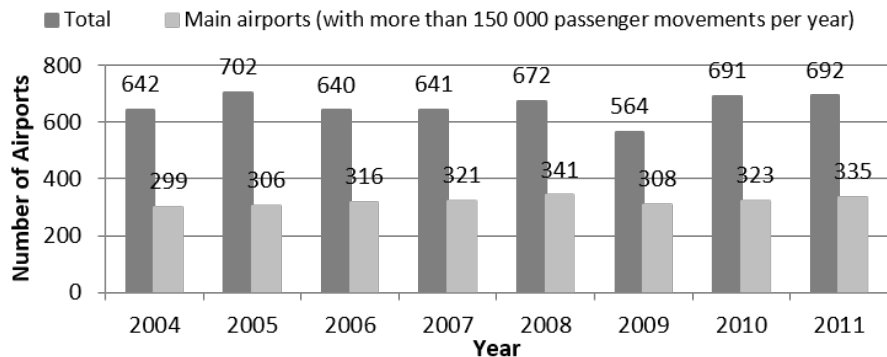


FIGURE 1.5: Number of airports (EUROSTAT)

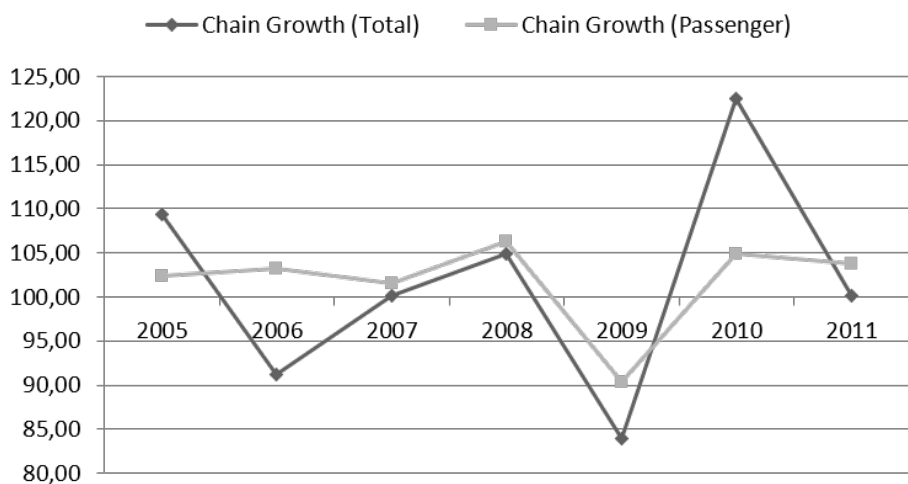


FIGURE 1.6: Growth rate. Number of airports (self study)

In order to show how air traffic will change, EUROCONTROL prepares medium and long term forecast for IFR movements. These forecasts are used mainly for planning purposes for airlines.

Long term forecast, published in June 2013 covers IFR flight movements for years 2013-2035. Because of the range, the forecast is more robust and is divided into four scenarios [3]

Scenario A: Global Growth (Technological Growth): Strong economic growth in an increasingly globalized World, with technology used successfully to mitigate the effects of sustainability challenges such as the environment or resources availability.

Scenario C: Regulated Growth: Moderate economic growth, with regulation reconciling the environmental, social and economic demands to address the growing global sustainability concerns. This scenario has been constructed as the most likely of the four, most closely following the trends.

Scenario C': Happy Localism: this scenario is introduced to investigate an alternative path for the future. With European economies being more and more fragile, increasing pressure on costs, stricter environmental constraints, air travel in Europe would adapt to new global environment but taking an inwards perspective. There would be less globalization, more trade inside EU (e.g. Turkey joining Europe is important in this scenario). Also, slow growth of leisure travel to outside Europe, however certainly more inside EU. More point-to-point traffic within Europe. It does not mean that Europe does not grow or does not adapt to new technologies and innovation but its main focus is local. Although this scenario is mostly based on scenario C (as its name indicates), it also inherits some aspects of other scenarios like higher fuel prices or low business aviation traffic of scenario D.

Scenario D: Fragmenting World: A World of increasing tensions between regions, with more security threats, higher fuel prices, reduced trade and transport integration and knock-on effects of weaker economies.

Scenario C: Regulated growth is considered to be the most likely at point of publishing the report. This forecast predicts 14.4 million flights in Europe 2035, which is 1.5 times more than in 2012. That creates an average growth of 1.8% per year. Forecast predicts that in 2025 traffic growth will decelerate due to predicted economic slowdown and reaching the capacity of airports.

As in medium term forecast, growth is not uniform across Europe. Due to lower starting point in calculations, more growth is expected in Eastern countries.

This however is not the full view on the situation. While growth will be faster in the East (figure 1.7), it is still mainly the big western countries that will need to deal with the greatest increase in the number of flights (figure 1.8).

Presented forecasts show, that air traffic in Europe will grow significantly in the next few years. With no actions taken, two paths are available. On one hand, running such traffic on existing fleet with airports (reaching maximum capacity) located near city centers will create an environment filled with constant aircraft noise. On a preventive side, noise emission regulations are being tightened nearly every year. And the only way to conform strict regulations is to use state of the art engines and airplanes, because in this case, silence is golden.

1.3 Some excerpts from airworthiness regulations

Any aircraft intended to carry people, both crew and passengers must fulfill rigorous airworthiness requirements including maximum stresses on the airframe, safety and

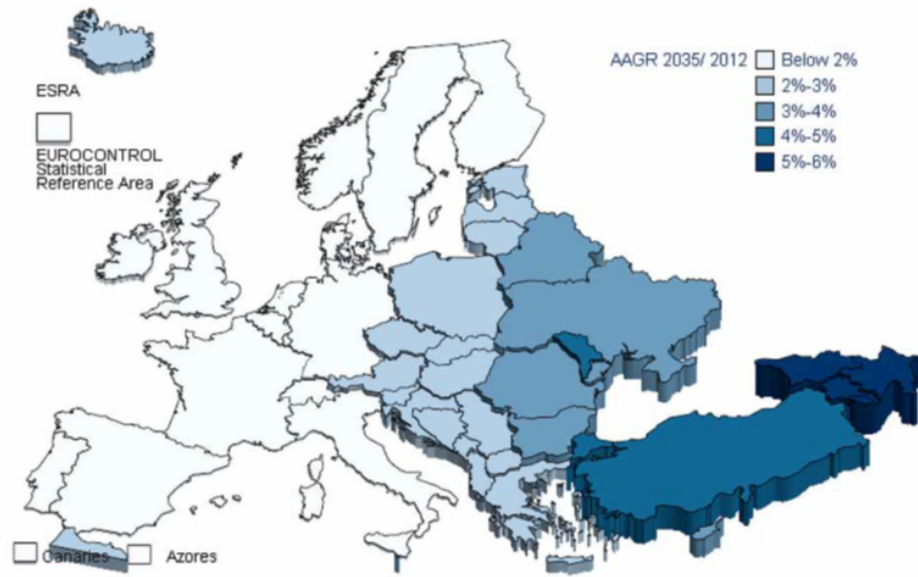


FIGURE 1.7: Average annual growth (scenario C: Regulated Growth) [2]

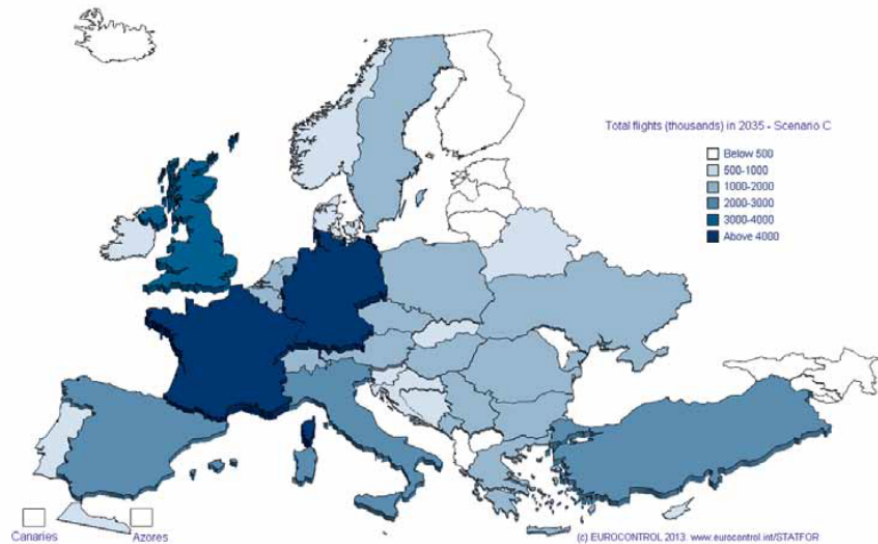


FIGURE 1.8: Total traffic in 2035 [2]

ecological impact induced while the aircraft is in use. Initially, the requirements were created by the country of origin of aircraft manufacturer, but since aerial operations become international and intercontinental, the airworthiness regulations evolved. Current airworthiness requirements are developed, introduced and maintained by international organizations such as ICAO. Excerpts from some top level requirements regarding generation of noise by aircraft at different stages of flight are presented in further sections.

1.3.1 CAEP regulations

ICAO's current environmental activities are largely undertaken through the Committee on Aviation Environmental Protection (CAEP), which was established by the Council in 1983, superseding the Committee on Aircraft Noise (CAN) and the Committee on Aircraft Engine Emissions (CAEE).

The current structure of the Committee includes three working groups and four support groups. The working groups deal with the technical and operational aspects of noise reduction and mitigation, with the aircraft noise and emissions issues linked to airports and operations and with the technical and operational aspects of aircraft emissions. One support group provides information on the economic costs and environmental benefits of the noise and emissions options considered by CAEP, one addresses models and databases issues, one deals specifically with the ICAO Carbon Calculator and the last one is aimed at scientific understanding of aviation environmental impacts.

About once a year, CAEP meets as a Steering Group to review and provide guidance on the progress of the activities of the working groups. So far, CAEP has held eight formal meetings: in 1986 (CAEP/1), 1991 (CAEP/2), 1995 (CAEP/3), 1998 (CAEP/4,) 2001 (CAEP/5), 2004 (CAEP/6), 2007 (CAEP/7) and 2010 (CAEP/8). Each formal CAEP meeting produces a report with specific recommendations for the consideration of the ICAO Council.

The Council acts on recommendations from CAEP in the light of any comments received from the Air Navigation Commission and, if there are economic aspects, from the Air Transport Committee. In the case of recommendations to introduce or amend Standards and Recommended Practices, there are established procedures for consulting States, after which the final decision rests with the Council.

1.3.2 ICAO Annex 16

Historically the oldest and presumably the most important regulations are stated in ICAO Annex 16 – Environmental Protection, Volume 1. First issue of this document was released in year 1981. At time of writing this article the latest issue is 6th, released in year 2011. Document contains standards (not strict requirements), Recommended Practices and Guide of the noise certification of aircraft that are operated in international air navigation, in accordance with the classification set out in the individual chapters. Each chapter describes different noise measurement points (Table 1.1) and noise levels for specific aircraft types:

- a) Annex 16 Chapter 2 describes requirements for subsonic, jet engine propelled air-craft certified before 6th November 1977. With exceptions;

- b) Annex 16 Chapter 3 describes requirements for:
- Subsonic, jet engine propelled aircraft certified between 6th November 1977 and 1st January 2006,
 - Propeller driven aircraft (MTOW over 8618 kg) certified between 1st January 1985 and 1st January 2006;
- c) Annex 16 Chapter 4 describes requirements for:
- Subsonic, jet engine propelled aircraft certified after 1st January 2006;
 - Propeller driven aircraft (MTOW over 8618 kg) certified after 1st January 2006.

Separate Chapters contain information on light aircraft (Annex 16 Chapter 7) and helicopters (Annex 16 Chapters 8 & 11) and will not be discussed.

Table 1.1 and 1.2 contain a brief summarize of maximum noise levels and their measurement points. Noise levels and measurement points are not rigid. Maximum noise levels are logarithmic dependent from Maximum Take-Off Weight (MTOW) of certified aircraft. Highest noise levels are for heavier aircraft, with MTOW above 385 000 kg. Annex 16 fully describes weather requirements, flight procedures and equipment setup for proper measurements. Noise levels are presented in EPNdB (Effective Perceived Noise dB). This unit is not measurable in a direct manner. EPNdB calculations are based on measurements of noise level (measurements of acoustical pressure), spectrum of noise level and corrected with sustainability factors and noise damping of air (also dependent on weather). Methods on how to establish a measurement point, calculate correction factors from weather, wind, inaccurate measurement point are described in Annex or in its Addenda. Data presented below is an excerpt from chapters 2, 3 and 4 from 6th edition of ICAO Annex 16 (Table 1.1).

Maximum noise levels gained from Annex 16 are below 108 EPNdB. In comparison: Heavy traffic generates around 85dB, pneumatic road drill - circa 100dB, live rock concert generates circa 110-115dB noise. Exposition to noise level higher than 110dB for over 15 minutes may result in hearing damage. Short term (less than 10 minutes) exposure to 120 results in hearing damage, 130 dB is considered as a threshold of pain, 150dB causes eardrum rapture, while 194dB is considered as theoretical limit for sound barrier at 1 atmosphere of pressure.

Noise levels appear to be high. But such levels occur only in the nearest vicinity of the airport. Concerning that nearly any main airport in Europe is surrounded by a large perimeter, nearest housing areas are subjected to noise levels that are safe, but may be considered as annoying. Also, many airports create their own noise requirements and do not allow air traffic operations of aircraft not conforming to such.

TABLE 1.1: Noise measurement points per ICAO Annex 16 [1]

Chapter	Noise measurement point		
	Name	Distance	Point
2	Sideway	650m	On line parallel to runway where measured noise is max
	Fly-by	6.5km	On extent of runway axis measured from start of take-off
	Approach	2000m	From runway threshold below approach path
3, 4	Sideway (jet)	450m	On line parallel to runway where measured noise is max
	Sideway (prop)	650m	Below take-off path for take-off power climb
	Fly-by	6.5km	On extent of runway axis measured from start of take-off
	Approach	2000m	From runway threshold below approach path

TABLE 1.2: Maximum noise levels per ICAO Annex 16 [1]

Chapter	Point	Engine count	Maximum EPNdB
2	Sideway	N/A	108-102
	Fly-by	N/A	108-93
	Approach	N/A	108-102
3, 4	Sideway	N/A 1 or 2	103-94 101-89
	Fly-by	3	104-89
		4	106-89
	Approach	N/A	105-98

1.3.3 Local regulations

One of the airports with most strict noise requirements is London Heathrow. It is the third busiest airport in the world, serving more than 70 million passengers in 2012 and handling more international passengers than any other airport in the world.

In order to prevent nearby housing areas from noise effects, particularly at night, Heathrow airport introduced their own regulations for incoming and departing traffic. Air traffic Control at Heathrow Approach Control guides traffic incoming from four major routes into one approach stream. When possible, Controllers advise the use of Continuous Descent Approach (CDA). CDA allows for a smooth, constant-angle descent to landing (Fig. 1.9). A continuous descent approach starts ideally from the top of descent, i.e. at cruise altitude, and allows the aircraft flying its individual optimal vertical profile down to runway threshold.

Night-time flights at Heathrow are subject to restrictions. Between 23:00 and 07:00, the noisiest aircraft (rated QC/8 and QC/16) cannot be scheduled for operation. In addition, during the night quota period (23:30–06:00) there are four limits:

- A limit on the number of flights allowed;

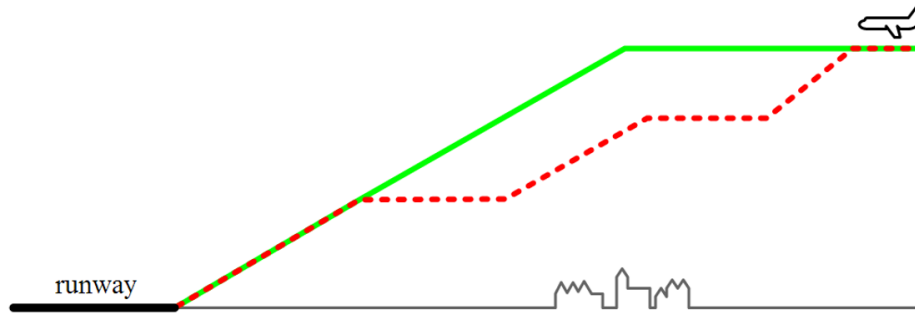


FIGURE 1.9: CDA approach (solid line) vs. Standard approach (dash line)

- A quota count system which limits the total amount of noise permitted, but allows operators to choose to operate fewer noisy aircraft or a greater number of quieter planes;
- QC/4 aircraft cannot be scheduled for operation;
- A voluntary agreement with the airlines that no early morning arrivals will be scheduled to land before 04:30.

A trial of "noise relief zones" ran from December 2012 to March 2013, which concentrated approach flight paths into defined areas compared with the existing paths which were spread out. The zones used alternated weekly, meaning residents in the "no-fly" areas received respite from aircraft noise for set periods. However, it was concluded that some residents in other areas experienced a significant dis-benefit as a result of the trial and that it should therefore not be taken forward in its current form.

The Quota Count (QC) system was introduced on Heathrow in 1993. Each aircraft is classified and awarded a grade, called a Quota Count, based on how much noise it generates. Quieter aircraft are given a smaller grade. Aircraft are classified separately for landing and take-off. Take-off quota count values are based on the average of the certificated flyover and sideline noise levels at maximum take-off weight, with 1.75 EPNdB added for ICAO Annex 16 Chapter 2 aircraft. Landing quota count values are based on the certificated approach noise level at maximum landing weight minus 9.0 EPNdB.

Noise classification for aircraft is described in Table 1.3. Examples of aircraft classified in the QC system are presented in Table 1.4.

Noise levels required by Heathrow Airport are far stricter than those stated in ICAO Annex 16. Such restrictions result in relatively noise friendly environment around Heathrow. ERCD report 1101 – Noise Exposure Contours for Heathrow Airport [18], prepared by Environmental Research and Consultancy Department of British Civil Aviation Authority shows the effect of Heathrow Airport traffic on nearby locations. Report

TABLE 1.3: Noise Quota Count classification in Heathrow [18]

Noise Classification	Quota Count
Below 84 EPNdB	Exempt
84-86.9 EPNdB	0.25
87-89.9 EPNdB	0.5
90-92.9 EPNdB	1
93-95.9 EPNdB	2
96-98.9 EPNdB	4
99-101.9 EPNdB	8
Greater than 101.9 EPNdB	16

prepared in year 2010, presents number and location of households affected by specific noise levels generated by Heathrow air traffic (Fig. 1.10).

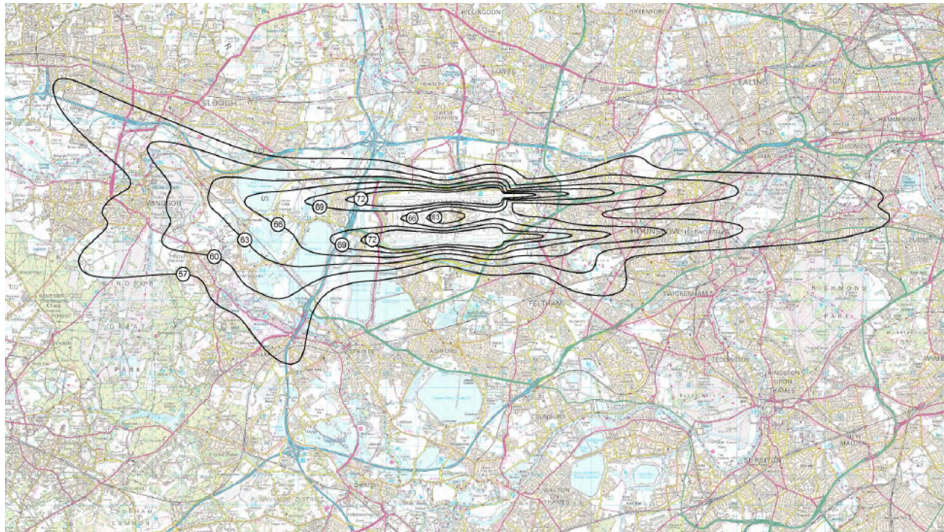


FIGURE 1.10: Heathrow noise contours. 83% western & 17% eastern traffic [18]

Noise contours (Fig. 1.10) show that 83dB of perceived noise level contains the terminal area, 72dB – in the nearest vicinity of the runway and 66dB outside the aerodrome premises. 60dB noise is comparable to normal office space or restaurant rustle. 70dB is the sound level of moderate traffic and may be annoying to some people.

This concludes that Heathrow airport restricts the movements of really loud airships to prevent its neighbors from aircraft noise. Presumably, Heathrow restrictions will lower the acceptable noise levels even more, due to increasing air traffic and urban sprawl around the airport.

TABLE 1.4: Examples of QC aircraft classification [18]

Aircraft type	QA Departure	QC Arrival
Airbus A320 family	0.5-1	0.25-0.5
Airbus A380	2	0.5
Boeing 737 Classic	0.25-0.5	1
Boeing 747-400	4	2
Boeing 747-8	2	1
Boeing 757-200	0.5	0.25
Boeing 767-300	1 - 2	1
Boeing 777-200ER	2	1
Embraer 145	0.25	0.25

1.4 Aircraft propulsion noise generation

Requirements described above are obviously relevant to an aircraft as a whole entity. In order to engineer a flying machine capable of fulfilling the stated requirements, one must identify the sources of noise within the aircraft in question.

Let's consider a "generic" airliner-kind of aircraft. Main sources of noise of such are the engines, aerodynamic surfaces and fuselage inducing turbulence and aerodynamically generated sound, APU as well as various internal aggregates (fuel and oil pumps, HVAC systems, electrical motors).

Research provided by Traub [28] gives an insight towards the components of noise generated by the aircraft during takeoff and landing, that is during two flight stages where the sound induced by aircraft is the most audible by the population on the ground. During the take-off phase, with engines set to maximum thrust generation, the fan noise and jet noise are the dominant components of the overall sound generation. During approach and landing phase, where engines are set to idle thrust, the dominant components are the engine fan and the airframe. The airframe noise is generated mostly by the extended high lift system generating flow of significant turbulence and vorticity 1.11.

The engine noise generation is distributed over its main components 1.11. A rather obvious conclusion arises. The more accessible the component is from the outside, the higher noise levels of the component are registered. Following that statement, for a large bypass turbofan engine, the impact of fan and exhaust jet is the most significant during the take-off and landing phase.

At this stage of study it can be assumed, that noise generation by the jet engine consists of three phenomena: noise generated by interaction of rotating machinery, combustion and combustion instability noise, and noise of mixing in shear layer in the exhaust jet. Detailed studies on sound generation by turbomachinery are found in set of articles in proceedings [17]. Details on combustion noise are presented in book [23].

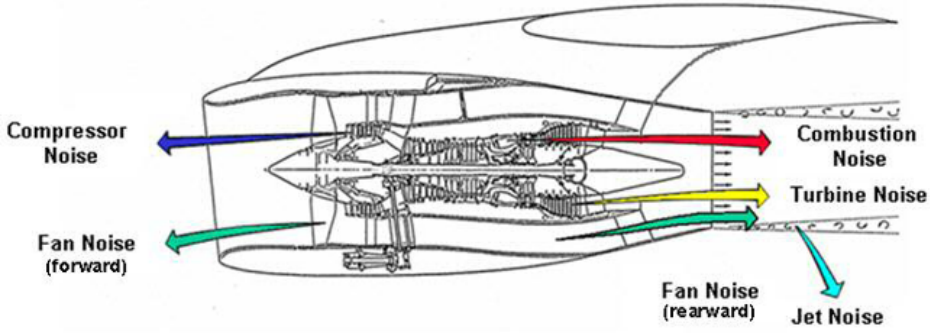


FIGURE 1.11: Sources of noise of a turbofan engine [28]

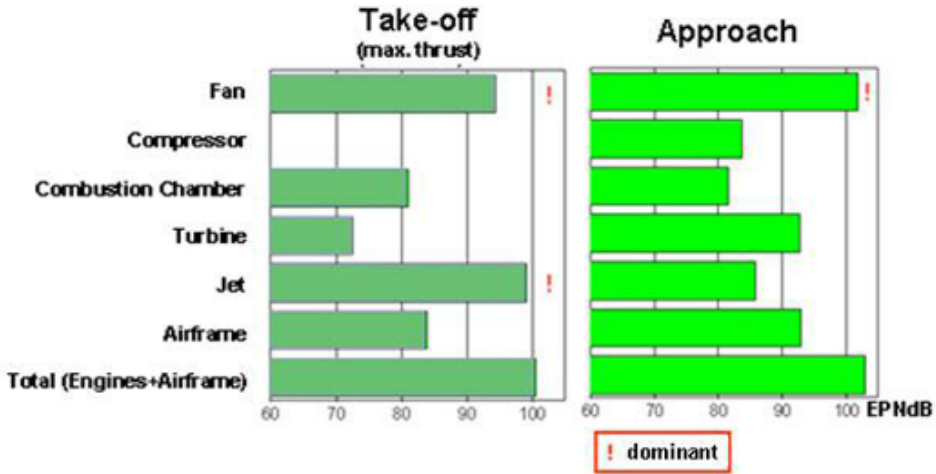


FIGURE 1.12: Impact of aircraft noise sources at take-off and landing [28]

Reducing the noise of a jet engine is a daring engineering task. Yet, the easiest element to handle with regard to noise emission is to reduce the sound emission of exhaust jet by introducing the additional turbulence degrading the mixing in the shear layer of the air stream behind the engine. This is achieved by introducing a minor modification to an engine nacelle and outlet nozzle that enforces rapid dissipation of the shear layer between the ambient air and the engine exhaust jet (fig. 1.13).

Implementation of a chevron enforces fluid motion, so that with minor (below 0.5%) decrease of thrust, achieving a decrease in EPNdB of a jet stream by 2.5 decibels, as performed on a scale tests performed by NASA (fig. 1.14) [16]. Such devices are becoming more popular in modern (or retrofitted) airliners in order to conform the strict requirements.

Reduction of noise generated by a fan requires deeper modifications to the engine construction. Both passive and active modifications to the fan rotor blading require extensive testing and certification on nearly all stages of the design process.



FIGURE 1.13: Engine nacelle chevron on a GEnx engine

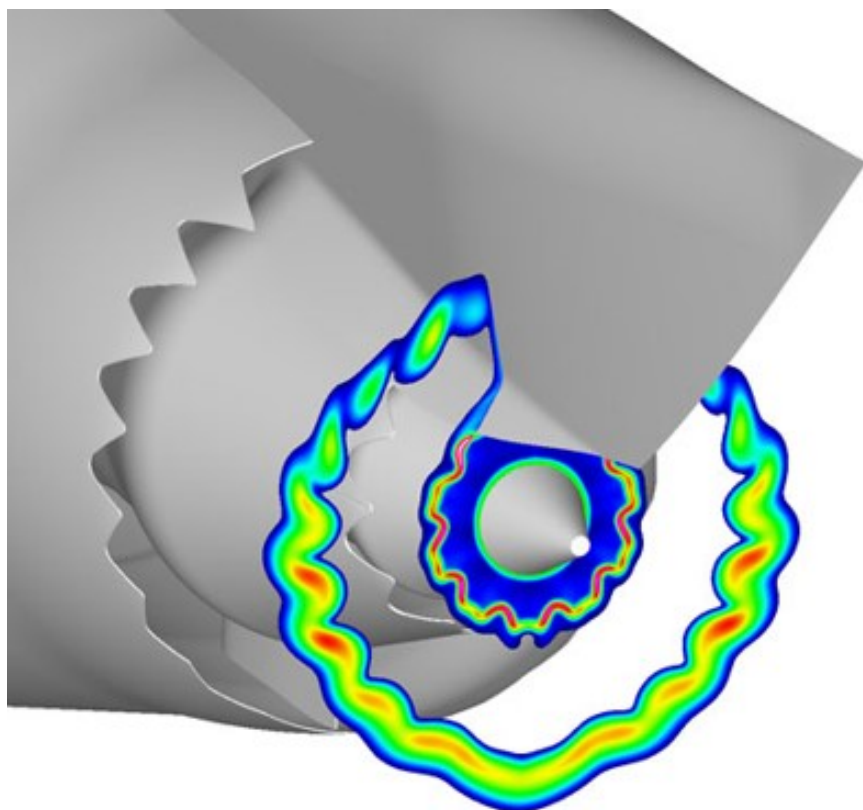


FIGURE 1.14: Exemplary anelysis on a chevron engine outlet [16]

Chapter 2

Current research on Computational Aeroacoustics

2.1 Classification of CAA methods

Computational aeroacoustics is a branch of aeroacoustics that aims to analyze the generation of noise by turbulent flows by means of numerical methods. A following classification of available methods is currently in use.

1. Hybrid Approach.
 - (a) Integral Method
 - i. Lighthill's Analogy
 - ii. Kirchoff Integral
 - iii. FW-H
 - (b) Linearized Euler Equations
 - (c) Pseudo Spectral
 - (d) EIF
 - (e) APE
2. Direct approach.

The direct approach is the core of this thesis and will be described in detail in chapter 3. A brief introduction to Lightill's analogy with Curle's modification is provided below. Ffowcs Williams Hawkings analogy as an extension to the theory is also provided.

2.2 Lighthill-Curle theory of aerodynamic sound

A mathematically formulated linkage between description of fluid flow and sound generation phenomena was proposed and solved by M. J. Lighthill. His work [19] focused on sound generation as a byproduct of airflow as distinct from sound generated by vibration of solids.

Consider a system with fluctuating flow occupying a very large volume of fluid, at which the non fluctuating part is at rest. Three mechanism of introducing kinetic energy to the system and transforming it to "acoustic energy" are following:

- I By forcing a mass of the fluid in a fixed region to fluctuate, as in the loudspeaker diaphragm
- II By forcing the momentum in fixed space to fluctuate or by forcing the rates of flux through a given control surface to vary, as in vibrating part of a machine (or after striking a tuning-fork)
- III By forcing the rates of flux through a given control surface to vary, without the vibrating motion of solid boundaries, as in noise generated turbulence in flow.

Efficiency of transformation the kinetic energy do sound decreases down the list. First two phenomena are well established in current knowledge and were described in many sources. The research on sound generated aerodynamically starts (probably) with aforementioned work [20].

Lighthill proposes, that Reynolds momentum equation (derived in chapter 3) already expresses that the momentum changes at exactly the same rate as if the medium was at rest under the combined action of real stresses and fluctuating Reynolds stresses. Uniform acoustic medium at rest experiences stresses only from variation of density proportional to the speed of sound squared. A Lighthill stress tensor is therefore introduced to describe the fluctuations of the fluid medium subject to acoustic stresses:

$$T_{ij} = \rho v_i v_j + P_{ij} - a_0^2 \rho \delta_{ij} \quad (2.1)$$

Term P_{ij} is the compression tensor defined as:

$$P_{ij} = (p - p_0) \delta_{ij} - \sigma_{ij} \quad (2.2)$$

where σ_{ij} is the stress tensor due to molecular viscosity defined by:

$$\sigma_{ij} \equiv \left[\mu \left(\frac{\partial \bar{u}_i}{\partial x_j} + \frac{\partial \bar{u}_j}{\partial x_i} \right) \right] - \frac{2}{3} \mu \frac{\partial \bar{u}_l}{\partial x_l} \delta_{ij} \quad (2.3)$$

Propagation of sound in fluid medium without external forces is presented by following governing equations:

$$\frac{\partial \rho}{\partial t} + \frac{\partial}{\partial x_i} (\rho v_i) = 0 \quad (2.4)$$

$$\frac{\partial}{\partial t} (\rho v_i) + a_0^2 \frac{\partial \rho}{\partial x_i} = 0 \quad (2.5)$$

$$\frac{\partial^2 \rho}{\partial t^2} - a_0^2 \nabla^2 \rho = 0 \quad (2.6)$$

The equation 2.4 is the continuity equation for a compressible fluid, equation 2.5 is an approximate equation of momentum and equation 2.6 is established by eliminating the ρv_i term from the previous equations.

By implementing the T_{ij} tensor to the equations 2.4 thru 2.6, the following form is obtained:

$$\frac{\partial \rho}{\partial t} + \frac{\partial}{\partial x_i} (\rho v_i) = 0 \quad (2.7)$$

$$\frac{\partial}{\partial t} (\rho v_i) + a_0^2 \frac{\partial \rho}{\partial x_i} = - \frac{\partial T_{ij}}{\partial x_j} \quad (2.8)$$

$$\frac{\partial^2 \rho}{\partial t^2} - a_0^2 \nabla^2 \rho = \frac{\partial^2 T_{ij}}{\partial x_i \partial x_j} \quad (2.9)$$

Therefore a term describing the fluctuations related to acoustic phenomena is now linked to the flow governing equations. It is now assumed, that resolving fluid flow along with the appropriate stress, strain and deformation terms can be now used to asses the sound phenomena in the flow field.

Should the receiver of the acoustical signal be outside the computational domain, further investigation must be concluded. Consider an unbounded flow field with a fluctuating point source, so that mass $Q(x, t)$ is introduced to the system at point x and time t , with total rate of introduction of $q(t)$. The density field is than given by the equation:

$$\rho - \rho_0 = \frac{1}{4\pi a_0^2} \frac{q' \left(\frac{t-r}{a_0} \right)}{r} \quad (2.10)$$

where r is the distance from source and $q'(t)$ is the time derivative of $q(t)$ and is defined as instantaneous source strength. For distributed source the equation 2.10 takes form:

$$\rho - \rho_0 = \frac{1}{4\pi a_0^2} \int \frac{\partial}{\partial t} Q \left(y, t - \frac{|x-y|}{a_0} \right) \frac{dy}{|x-y|} \quad (2.11)$$

The equation 2.11 is then solved to a form:

$$\rho - \rho_0 = \frac{1}{4\pi a_0^2} \frac{\partial^2}{\partial x_i \partial x_j} \int T_{ij} \left(y, t - \frac{|x-y|}{a_0} \right) \frac{dy}{|x-y|} \quad (2.12)$$

The equation 2.12 considers an unbounded flow field with point or volumetric source of fluctuations considered as quadrupole sources of acoustic fluctuations. This concept was evolved by Curle [13] to include the effect of solid boundaries on their reflection and diffraction. The modification of the original equation 2.12 is:

$$\begin{aligned} \rho - \rho_0 &= \frac{1}{4\pi a_0^2} \frac{\partial^2}{\partial x_i \partial x_j} \int_V T_{ij} \left(y, t - \frac{r}{a_0} \right) \frac{dy}{r} \\ &\quad - \frac{1}{4\pi a_0^2} \frac{\partial}{\partial x_i} \int_S P_i \left(y, t - \frac{r}{a_0} \right) \frac{dS(y)}{r} \end{aligned} \quad (2.13)$$

where:

$$P_i = -l_j P_{ij} \quad (2.14)$$

where: $l_i = (l_1, l_2, l_3) = n$ is the direction cosines of the outward normal from the fluid, and the sound generated in a medium at rest by a distribution of dipoles of strength P_i per unit area and therefore P_i is the force per unit area exerted on the fluid by the solid boundaries in the x_i direction.

2.3 FW-H Analogy

Further development of analogies developed in references [19], [20] and [13] is presented in work [33]. The extension to the theory includes the effect of arbitrary convective motion of fluid. More over, the FW-H analogy switches from Lighthill's unbounded fluid to a bounded volume. Thus it is possible to compute the flow phenomena within the acoustic near field (which in this case would be a CFD domain) and compute the sound propagation outwards to the acoustic far field (outside the CFD domain) using wave propagation equations.

FW-H analogy derives it's governing equation from a volume of fluid V enclosed by a surface Σ , divided into regions 1 and 2 with surface of the discontinuity S moving into region 2 with velocity v . By formulating the rate of change of mass within volume V and deriving a generalized continuity and momentum equations, an equation governing the generation and propagation of sound is obtained.

$$\left(\frac{\partial^2}{\partial t^2} - a^2 \frac{\partial^2}{\partial x_i^2} \right) (\overline{\rho - \rho_0}) = \frac{\partial^2 \overline{T_{ij}}}{\partial x_i \partial x_j} - \frac{\partial}{\partial x_i} \left(P_{ij} \delta(f) \frac{\partial f}{\partial x_j} \right) + \frac{\partial}{\partial t} \left(\rho_0 v_i \delta(f) \frac{\partial f}{\partial x_i} \right) \quad (2.15)$$

where: $(\overline{\rho - \rho_0})$ is the generalized density perturbation - the amplitude of sound and $\overline{T_{ij}}$ is equal to T_{ij} (eq. 2.1) outside any surfaces and equal 0 when within them. Equation $f = 0$ defines the division surface surface S , such that $f < 0$ is in the region 1 and $f > 0$ in region 2 (Heavyside function). The $\delta(f)$ is the Dirac delta function.

The equation 2.15 shows that sound can be regarded as generated by three source distributions: in volume - the quadrupole distribution of strength T_{ij} , on surface - the distribution of dipoles of strength density $P_{ij}n_j$ and monopole distributions from the displacement of volume by the moving surface.

Equation 2.15 can be rewritten to a different form:

$$\begin{aligned} \frac{1}{a_0^2} \frac{\partial^2 (p')}{\partial t^2} - \nabla^2 (p') &= \frac{\partial^2}{\partial x_i \partial x_j} \{ T_{ij} H(f) \} \\ &- \frac{\partial}{\partial x_i} \{ [P_{ij} n_j + \rho u_i (u_n - v_n)] \delta(f) \} \\ &+ \frac{\partial}{\partial t} \{ [\rho_0 v_n + \rho (u_n - v_n)] \delta(f) \} \end{aligned} \quad (2.16)$$

where:

$p' = p - p_0$ — sound pressure fluctuation

u_i — fluid velocity in the x_i direction

u_n — fluid velocity component normal to the surface $f = 0$

v_i — surface velocity in the x_i direction

v_n — surface velocity component normal to the surface

$H(f)$ — Heaviside function

$\delta(f)$ — Dirac delta function

The rewritten equation 2.16 represents an inhomogeneous wave equation can be integrated under specific assumptions and the solutions consists of surface (monopole and dipole sources) and volume integrals (quadrupole sources). Software package used

for further computations omits the effect of volume integral, therefore the result is of following form:

$$p'(x, t) = p'_T(x, t) + p'_L(x, t) \quad (2.17)$$

with further development of the solution:

$$\begin{aligned} 4\pi p'_T(x, t) &= \int_{f=0} \left[\frac{\rho_0 (\dot{U}_n + U_{\dot{n}})}{r (1 - M_r)^2} \right] dS \\ &+ \int_{f=0} \left[\frac{\rho_0 U_n \{ r \dot{M}_r + a_0 (M_r - M^2) \}}{r^2 (1 - M_r)^3} \right] dS \end{aligned} \quad (2.18)$$

$$\begin{aligned} 4\pi p'_L(x, t) &= \frac{1}{a_0} \int_{f=0} \left[\frac{\dot{L}_r}{r (1 - M_r)^2} \right] dS \\ &+ \int_{f=0} \left[\frac{L_r - L_M}{r^2 (1 - M_r)^2} \right] dS \\ &+ \frac{1}{a_0} \int_{f=0} \left[\frac{L_r \{ r \dot{M}_r + a_0 (M_r - M^2) \}}{r^2 (1 - M_r)^3} \right] dS \end{aligned} \quad (2.19)$$

where:

$$U_i = v_i + \frac{\rho}{\rho_0} (u_i - v_i) \quad (2.20)$$

$$L_i = P_{ij} n_j + \rho v_i (u_i - v_i) \quad (2.21)$$

When the integration surface coincides with an impenetrable wall, the two terms equation 2.17, $p'_T(x, t)$ and $p'_L(x, t)$ are often referred to as thickness and loading terms, respectively, in light of their physical meanings. The square brackets in equations 2.18 and 2.19 denote that the kernels of the integrals are computed at the corresponding retarded times, τ , defined as in equation 2.22, given the receiver time, t , and the distance to the receiver, r .

$$\tau = t - \frac{r}{a_0} \quad (2.22)$$

The various subscripted quantities appearing in equations 2.18 and 2.19 are the inner products of a vector and a unit vector implied by the subscript. For instance, $L_r = \vec{L} \cdot \vec{r} = L_i r_i$ and $U_n = \vec{U} \cdot \vec{n} = U_i n_i$, where \vec{r} and \vec{n} denote the unit vectors in the radiation and wall-normal directions, respectively. The Mach number vector M_i in equations 2.18 and 2.19 relates to the motion of the integration surface: $M_i = \frac{v_i}{a_0}$. The L_i quantity is a scalar product $L_i M_i$. The dot over a variable denotes source-time differentiation of that variable [4] [33] [9].

FW-H analogy is therefore the general form of Lighthill's acoustic analogy for aerodynamically generated noise, including volume sources of quadrupole kind, such as turbulence in free stream, and dipole and monopole sources of the moving solid body surface within the flow. Solution of the governing equation 2.15 given in equations 2.17, 2.19 & 2.18 omits the sources as weak.

2.4 Limitations to acoustic analogies

Hybrid methods, including the presented Ffowcs Williams – Hawking analogy provide a computationally efficient task for engineering problems such as airframe noise, noise of jet injection to ambient medium at rest (that is jet engine noise problem), effect of wake generated by automobile mirror on noise in the vehicle cabin. The solution to the FW-H governing equation presented in equations 2.18 and 2.19 may reach instability when the Mach number in the sound radiation direction M_r approaches 1, that is: when the freestream flow velocity approaches sonic conditions. Using the hybrid approach with acoustic analogies may be challenging and poses a risk of obtaining "non-physical" results for case considered in this thesis, that is blade of axial compressor in stationary reference frame.

For phenomena characteristic to axial compressor flow, that is strong shockwaves, shockwave with boundary layer interaction, high separation of flow enforced by shock waves, and high adverse pressure gradient may cause mathematical and numerical instabilities to the solution. Considering the pressure change within the computational domain, or, from the governing equation's standpoint, the volume enclosed by a surface, poses some difficulty to choosing free-stream values of density and pressure.

Further attempts towards gaining insight of the sound generation phenomena shall be performed by attempting to use a direct formulation method.

Chapter 3

Approach and direct formulation of noise analysis

3.1 Direct formulation of noise analysis

The intention behind this study is to perform a flow field noise analysis in CFD without implementation of acoustical analogies to the CFD code itself. Moreover, very limited information on direct formulation of noise analysis was found during the research, with even fewer research on acoustical nearfield of transonic axial compressors or axial fans of twin spool jet engines.

The process for the direct formulation noise analysis is following:

1. Obtain raw flowfield data of static pressure, velocity magnitude from CFD analysis,
2. Perform averaging over time of pressure and velocity magnitude for each point or cell in the flowfield (equation 3.1),
3. Obtain offset from mean static pressure and velocity magnitude for every timestep for every point/cell in the saved flow field (equation 3.2).

$$\bar{p} = \frac{1}{n} \sum_{n=1}^N p_k \quad \text{and} \quad \bar{u} = \frac{1}{n} \sum_{n=1}^N u_k \quad (3.1)$$

$$p_{k \text{ sound}} = p_k - \bar{p} \quad \text{and} \quad u_{k \text{ particle}} = u_k - \bar{u} \quad (3.2)$$

Sound pressure signal and flow velocity offset is obtained for every node or cell centroid throughout the simulation flowtime. This dataset can be now post processed. Dataset obtained in described manner now contains sound pressure in the flowfield in

every mesh node or cell centroid throughout the computational time. The dataset is now post processed to obtain quantity information of the acoustic nearfield.

Sound intensity for cells/nodes in fluid volume is calculated using formula 3.3.

$$I_k = p_{k \text{ sound}} \cdot u_{k \text{ particle}} \quad (3.3)$$

RMS sound pressure level and intensity level can be obtained from the respective data with use of the formula 3.4.

$$p_{rms} = \sqrt{\frac{\sum_{n=1}^N p_{k \text{ sound}}^2}{N}} \quad I_{rms} = \sqrt{\frac{\sum_{n=1}^N u_{k \text{ particle}}^2}{N}} \quad (3.4)$$

Sound pressure decibel level (SPLdB) for time specific $p_{k \text{ sound}}$ values and RMS values p_{rms} is computed using formula 3.5 with standard reference pressure $p_{ref} = 20\mu Pa$, whereas for sound intensity with formula 3.6 and with reference intensity $I_{ref} = 1pW/m^2$.

$$SPLdB = 20 \cdot \log_{10} \left(\frac{|p_{k \text{ sound}}|}{p_{ref}} \right) \quad (3.5)$$

$$SILdB = 10 \cdot \log_{10} \left(\frac{|I_k|}{I_{ref}} \right) \quad (3.6)$$

The signal obtained by direct approach is stored in discrete samples. Using a continuous Fourier Transform would require approximation of the sampled signal to a continuous function, which for large datasets is unjustified. In order to obtain ordinary sinuses of the acoustic signal a Discrete Fourier Transform is performed (eq. 3.7).

$$X_k = \sum_{n=0}^{N-1} x_n \cdot e^{-\frac{j2\pi kn}{N}} \quad (3.7)$$

Let's assume that:

$$b_n = \frac{2\pi kn}{N} \quad (3.8)$$

Therefore, the equation 3.7 can be written as:

$$X_k = x_0 e^{-jb_0} + x_1 e^{-jb_1} + x_2 e^{-jb_2} + \dots + x_{N-1} e^{-jb_{N-1}} \quad (3.9)$$

Using Euler's identity the exponent is decomposed (eq. 3.10) to a complex sum:

$$e^{jx} = \cos(x) + j \cdot \sin(x) \quad (3.10)$$

Therefore the equation 3.7 can be written as:

$$X_k = x_0[\cos(-b_0) + j \sin(-b_0)] + \dots + x_{N-1}[\cos(-b_{N-1}) + j \sin(-b_{N-1})] \quad (3.11)$$

Rearranging the equation 3.11 and summing up the real and imaginary components will return a complex vector X_k for "k-th" frequency bin.

$$X_k = A_k + jB_k \quad (3.12)$$

The frequency resolution of the DFT depends on the sampling frequency and number of samples, and is calculated by formula 3.13.

$$f_{bin} = \frac{f_s}{N} \quad (3.13)$$

Fourier coefficients are then used to compute the amplitude (eq. 3.14) and phase shift (eq. 3.15) for the "k-th" frequency bin ordinary sinus.

$$\text{Amp}_k = 2 \cdot \sqrt{A_k^2 + B_k^2} \cdot \frac{1}{N} \quad (3.14)$$

$$\theta_k = \arctan \frac{B_k}{A_k} \quad (3.15)$$

3.2 CFD analysis requirements

References [19], [20], [33] and [13] provide a theoretical insight on generating sound in fluid flow due to shear mixing of flows or by implementing a solid boundary in the flow. General remark is: any source of turbulence that result in pressure fluctuation will result in generating sound. Therefore the main requirement for CFD analysis used in direct approach noise analysis is the capability of resolving turbulent flow and corresponding fluctuations of pressure.

Let's consider the effect of injection of energy to the fluid resulting in creation of eddies (Fig. 3.1). Once the energy is injected to the fluid, a large scale eddy is formed and due to the fluid viscosity the eddy dissipates along with the dissipation of energy up to the point where the particle movement is considered as heat.

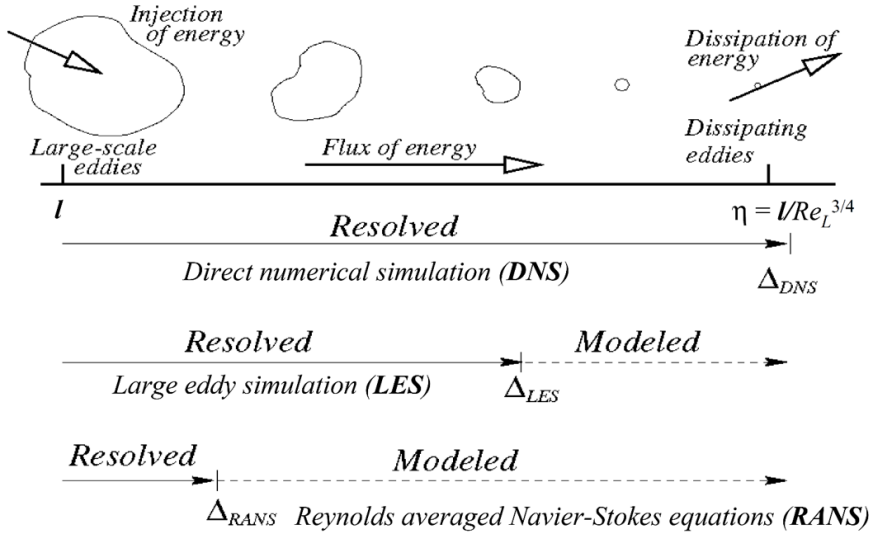


FIGURE 3.1: Resolving eddies in different kinds of CFD analyses

3.2.1 Governing equations

Computational fluid dynamics is based upon two equations governing the motion and deformation of the fluid: the continuity (3.16) and momentum (3.17) equations.

$$\frac{\partial \rho}{\partial t} + \nabla(\rho U) = 0 \quad (3.16)$$

$$\frac{dU}{dt} = -\frac{1}{\rho} \nabla p + \nu \nabla^2 U \quad (3.17)$$

In order to solve the governing equations in a computational grid, using a software system that is incapable of solving partial differential equations, a set of special treatments must be conducted to the equations. Problems regarding the formulation, discretization, preconditioning and solving the equations can be found in many literature sources [6], [30], [4].

3.2.2 Direct Numerical Simulation

Considering the direct formulation of noise, the Direct Numerical Simulation is seemingly the best tool of choice. The DNS formulation of flow solves directly the discrete form of Navier-Stokes Equation with direct resolving of turbulent flows. Size limit of the resolved eddies is the Kolmogorov limit (eq. 3.18). In order to properly resolve the DNS simulation up to this scale, the mesh sizing must be at least as small as the expected Kolmogorov limit at given Reynolds number.

$$\eta \approx \frac{l}{Re^{3/4}} \quad (3.18)$$

Reference [10] provides information on calculating the mesh grid node count for DNS calculations (eq. 3.19) for flat plate airfoil of aspect ratio L_z/L_x . The computational box for this case is of size $L_x \times \delta \times L_z$ in streamwise, normal to plate and spanwise direction respectively, where δ is the boundary layer thickness.

$$N_{DNS} = 0.000153 \frac{L_z}{L_x} Re_{L_x}^{37/14} \left[1 - \left(\frac{Re_{x_0}}{Re_{L_x}} \right)^{23/14} \right] \quad (3.19)$$

Point x_0 is the location where formulas 3.20 and 3.21 are valid for Reynolds number range ($10^6 \leq Re_x \leq 10^9$).

$$\delta = x \cdot 0.16 Re_x^{(-1/7)} \quad (3.20)$$

$$c_f = 0.027 Re_x^{(-1/7)} \quad (3.21)$$

For aspect ratio $L_z/L_x = 4$ and $Re_{x_0} = 5 \cdot 10^5$ the node count for streamwise $Re = 10^6$ is roughly $2.99 \cdot 10^{12}$ nodes and for $Re = 10^7$ is roughly $1.92 \cdot 10^{15}$ nodes.

Such node and cell counts are impossible to solve within practical walltime, therefore usage of DNS for sound analysis is limited to small (10^3) Reynolds numbers.

3.2.3 Large Eddy Simulation

Large eddy simulation (LES) is a mathematical model for modeling turbulent flows used in computational fluid dynamics. It was initially proposed in 1963 by Joseph Smagorinsky to simulate atmospheric air currents [24].

The principal idea behind LES is to reduce the computational cost by ignoring the smallest length scales, which are the most computationally expensive to resolve, via low-pass filtering of the Navier–Stokes equations. Such a low-pass filtering, which can be viewed as a time- and spatial-averaging, effectively removes small-scale information from the numerical solution. This information is not irrelevant, however, and its effect on the flow field must be modeled, a task which is an active area of research for problems in which small-scales can play an important role, such as acoustics [31].

The governing equations employed for LES are obtained by filtering the time dependent Navier-Stokes equations in either Fourier (wave-number) space or configuration (physical) space. The filtering process effectively filters out the eddies whose scales are

smaller than the filter width or grid spacing used in the computations. The resulting equations therefore governs the dynamics of large eddies [4].

A filtered variable is defined by:

$$\bar{\phi}(x) = \int_D \phi(x') G(x, x') dx' \quad (3.22)$$

where D is the fluid domain, and G is the filter function that determines the scale of the resolved eddies. The finite volume discretization itself implicitly provides the filtering operation:

$$\bar{\phi}(x) = \frac{1}{V} \int_{\nu} \phi(x') dx', \quad x' \in \nu \quad (3.23)$$

where V is the volume of a computational cell. The filter function, $G(x, x')$ implied here is then:

$$G(x, x') = \begin{cases} \frac{1}{V}, & \text{if } x' \in \nu \\ 0, & \text{otherwise} \end{cases} \quad (3.24)$$

For compressible flows, it is convenient to introduce the density-weighted (or Favre) filtering operator:

$$\tilde{\phi} = \frac{\overline{\rho\phi}}{\overline{\phi}} \quad (3.25)$$

Filtering the continuity 3.16 and momentum 3.17 equations following form is obtained:

$$\frac{\partial \rho}{\partial t} + \frac{\partial}{\partial x_i} (\rho \bar{u}_i) = 0 \quad (3.26)$$

$$\frac{\partial}{\partial t} \rho \bar{u}_i + \frac{\partial}{\partial x_j} (\rho \bar{u}_i \bar{u}_j) = \frac{\partial}{\partial x_j} (\sigma_{ij}) - \frac{\partial \bar{p}}{\partial x_i} - \frac{\partial \tau_{ij}}{\partial x_j} \quad (3.27)$$

where σ_{ij} is the stress tensor due to molecular viscosity defined by:

$$\sigma_{ij} \equiv \left[\mu \left(\frac{\partial \bar{u}_i}{\partial x_j} + \frac{\partial \bar{u}_j}{\partial x_i} \right) \right] - \frac{2}{3} \mu \frac{\partial \bar{u}_l}{\partial x_l} \delta_{ij} \quad (3.28)$$

and τ_{ij} is the subgrid-scale stress defined by:

$$\tau_{ij} \equiv \rho \bar{u}_i \bar{u}_j - \rho \bar{u}_i \bar{u}_j \quad (3.29)$$

The Favre Filtered Navier-Stokes equation takes the same form as equation 3.27. The compressible form of the subgrid stress tensor is defined as:

$$\tau_{ij} = \bar{\rho} u_i \tilde{u}_j - \bar{\rho} \tilde{u}_i \tilde{u}_j \quad (3.30)$$

The subgrid-scale stresses resulting from the filtering operation are unknown, and require modeling. The subgrid-scale turbulence models employ the Boussinesq hypothesis [15] in the RANS models, computing subgrid-scale turbulent stresses from:

$$\tau_{ij} - \frac{1}{3} \tau_{kk} \delta_{ij} = -2\mu_t \bar{S}_{ij} \quad (3.31)$$

where μ_t is the subgrid-scale turbulent viscosity. The isotropic part of the subgrid-scale stresses τ_{kk} is not modeled, but added to the filtered static pressure term. S_{ij} is the rate-of-strain tensor for the resolved scale defined by:

$$\bar{S}_{ij} \equiv \frac{1}{2} \left(\frac{\partial \bar{u}_i}{\partial x_j} + \frac{\partial \bar{u}_j}{\partial x_i} \right) \quad (3.32)$$

Equation 3.30 is split into its isotropic and deviatoric parts:

$$\tau_{ij} - \frac{1}{3} \tau_{kk} \delta_{ij} = -2\mu_t \left(S_{ij} - \frac{1}{3} S_{kk} \delta_{ij} \right) \quad (3.33)$$

Using LES approach is viable for resolving directly formulated noise, yet the computational cost of such calculations is still relatively large due to mesh sizing requirements. As stated by [10] the required node count for the analysis can be described by formulas 3.34 and 3.35 for modeled and resolved boundary layers respectively.

$$N_{wm} = 54.7 \frac{L_z}{L_x} n_x n_y n_z Re_{L_x}^{2/7} \left[\left(\frac{Re_{L_x}}{Re_{x_0}} \right)^{(5/7)} - 1 \right] \quad (3.34)$$

$$N_{wr} = 0.021 \frac{n_y}{\Delta x_w^+ \Delta z_w^+} \frac{L_z}{L_x} Re_{L_x}^{13/7} \left[1 - \left(\frac{Re_{L_x}}{Re_{x_0}} \right)^{(6/7)} \right] \quad (3.35)$$

The computational box for this case is of size $L_x \times \delta \times L_z$ in streamwise, normal to plate and spanwise direction respectively, where δ is the boundary layer thickness.

For $L_z/L_x = 4$ and $Re_{x_0} = 5 \cdot 10^5$ the node count for streamwise $Re = 10^6$ and $Re = 10^7$ is computed. The $n_x n_y n_z$ product is the number of grid points to resolve the cubic computational volume δ^3 exterior to the viscous wall region. Suggested value of $n_x n_y n_z = 2500$, where $n_x = 10$ $n_y = 25$ $n_z = 10$ was used for the computation of node

count with equation 3.34. Suggested $\Delta x_w^+ \approx 100$, $\Delta z_w^+ \approx 20$ and $n_y \approx 10$ was used for computation of node count with equation 3.35.

Node count for $Re = 10^6$ is roughly $1.82 \cdot 10^7$ nodes for modelled and $2.61 \cdot 10^7$ nodes for resolved wall flow. For $Re = 10^7$ the figures are $4.10 \cdot 10^8$ and $3.88 \cdot 10^9$ nodes respectively [10].

It must be noted that provided cell count is solely for a flow box of boundary layer width. Respective mesh sizing should be propagated towards volume of the computational domain thus enlarging the mesh even further.

LES analyses are commonly used in research and engineering and the method used is feasible for the direct noise formulation. The computational expense of the LES analysis is high, although manageable. It must be noted, that at time of performing this study the resources to carry out the analysis of that kind were unavailable to the author. Second limiting factor for LES is the amount of data generated during the process. As the direct approach requires storing at least every second time step for further processing, terabytes of data are predicted.

3.2.4 Reynolds Averaged Navier Stokes

The most computationally efficient method for resolving turbulent flows is using Reynolds Averaged Navier Stokes equation.

Consider a conservation variable ϕ of fluid described by spatial and temporal variables. The quantity may be decomposed to a sum of time averaged value in given spatial coordinates and time dependent fluctuations (eq. 3.36).

$$\phi(x, y, z, t) = \overline{\phi(x, y, z, t)} + \phi'(x, y, z, t) \quad (3.36)$$

Consider at first the continuity equation 3.16. By applying Reynolds decomposition to velocity vector we obtain:

$$\frac{\partial \rho}{\partial t} + \frac{\partial \overline{\rho u_i}}{\partial x_i} + \frac{\partial \rho u'_i}{\partial x_i} = 0 \quad (3.37)$$

By averaging the both sides of the equation 3.37 and applying averaging rules to its components we obtain:

$$\frac{\partial \rho}{\partial t} + \frac{\partial \overline{\rho u_i}}{\partial x_i} + \frac{\partial \overline{\rho u'_i}}{\partial x_i} = 0 \quad (3.38)$$

Because the average of an average is equal average, and the average of the fluctuation component is equal 0 we obtain equation 3.39, the Reynolds averaged continuity equation.

$$\frac{\partial \rho}{\partial t} + \frac{\partial \rho u_i}{\partial x_i} = 0 \quad (3.39)$$

By taking the momentum equation 3.17, switching to the index notation and applying the Reynolds decomposition we obtain the equation 3.40

$$\underbrace{\frac{\partial (\bar{u}_i + u'_i)}{\partial t}}_1 + \underbrace{(\bar{u}_j + u'_j) \frac{\partial (\bar{u}_j + u'_j)}{\partial x_j}}_2 = - \underbrace{\frac{1}{\rho} \frac{\partial (\bar{p} + p')}{\partial x_i}}_3 + \nu \underbrace{\frac{\partial^2 (\bar{u}_i + u'_i)}{\partial x_j^2}}_4 \quad (3.40)$$

Components 1, 3 and 4 of the above equation are treated in the same manner as the continuity equation and thus we obtain:

$$\underbrace{\frac{\partial \bar{u}_i}{\partial t}}_1 \quad \underbrace{\frac{1}{\rho} \frac{\partial \bar{p}}{\partial x_i}}_3 \quad \underbrace{\nu \frac{\partial^2 \bar{u}_i}{\partial x_j^2}}_4 \quad (3.41)$$

The decomposition of component 2 from the equation 3.40 requires multiplication of the components within the braces and performing Reynolds averaging on each of the products:

$$\underbrace{\left((\bar{u}_j + u'_j) \cdot \frac{\partial (\bar{u}_i + u'_i)}{\partial x_j} \right)}_2 = \underbrace{\left(\bar{u}_j \frac{\partial \bar{u}_i}{\partial x_j} \right)}_{M \cdot M \neq 0} + \underbrace{\left(\bar{u}_j \frac{\partial u'_i}{\partial x_j} \right)}_{M \cdot F = 0} + \underbrace{\left(u'_j \frac{\partial \bar{u}_i}{\partial x_j} \right)}_{F \cdot M = 0} + \underbrace{\left(u'_j \frac{\partial u'_i}{\partial x_j} \right)}_{F \cdot F \neq 0} \quad (3.42)$$

The $F \cdot F \neq 0$ product can be further simplified by equation:

$$\frac{\partial u'_j u'_i}{\partial x_j} = \underbrace{u'_i \frac{\partial u'_j}{\partial x_j}}_{= 0} + \underbrace{u'_j \frac{\partial u'_i}{\partial x_j}}_{F \cdot F \neq 0} \quad (3.43)$$

By inserting the components 1 through 4 from equations 3.41 and 3.42 modified by equation 3.43 to the equation 3.40 we obtain the Reynolds averaged momentum equation:

$$\frac{d\bar{U}}{dt} = - \frac{1}{\rho} \frac{\partial \bar{p}}{\partial x_i} + \frac{\partial}{\partial x_j} \left[\nu \frac{\partial \bar{u}_j}{\partial x_j} - \bar{u}'_i \bar{u}'_j \right] \quad (3.44)$$

By representing the viscous terms as a stress tensor (eq. 3.45) we obtain the momentum equation with turbulent stress (eq 3.46)

$$\nu \frac{\partial^2 \bar{u}_i}{\partial x_j^2} = \frac{1}{\rho} \frac{\partial}{\partial x_j} \tau_{ij} \quad (3.45)$$

$$\frac{d\bar{U}}{dt} = -\frac{1}{\rho} \nabla \bar{p} + \frac{1}{\rho} \frac{\partial}{\partial x_j} \left[\tau_{ij} - \rho \bar{u}'_i \bar{u}'_j \right] \quad (3.46)$$

The $\rho \bar{u}'_i \bar{u}'_j$ term can be further transformed to Reynolds stress tensor linked to shear stress.

The remaining fluctuating component is then modeled rather than resolved, by one of many turbulence model based on Bousinessque theory.

3.2.5 Hybrid RANS/LES Methods

At first, the concepts of Reynolds Averaging and Spatial Filtering seem incompatible, as they result in different additional terms in the momentum equations (Reynolds Stresses and sub-grid stresses). This would preclude hybrid models like Scale-Adaptive Simulation (SAS), Detached Eddy Simulation (DES), Shielded DES (SDES), or Stress-Blended Eddy Simulation (SBES), which are based on one set of momentum equations throughout the RANS and LES portions of the domain. However, it is important to note that once a turbulence model is introduced into the momentum equations, they no longer carry any information concerning their derivation (averaging). Case in point is that the most popular models, both in RANS and LES, are eddy viscosity models that are used to substitute either the Reynolds- or the sub-grid stress tensor. After the introduction of an eddy viscosity (turbulent viscosity), both the RANS and LES momentum equations are formally identical. The difference lies exclusively in the size of the eddy-viscosity provided by the underlying turbulence model. This allows the formulation of turbulence models that can switch from RANS to LES mode, by lowering the eddy viscosity in the LES zone appropriately, without any formal change to the momentum equations [4].

For further calculations, Delayed Detached Eddy Simulation with $k - \omega SST$ model was chosen. In the DES approach, the unsteady RANS models are employed in the boundary layer, while the LES treatment is applied to the separated regions. The LES region is normally associated with the core turbulent region where large unsteady turbulence scales play a dominant role. In this region, the DES models recover LES-like subgrid models. In the near-wall region, the respective RANS models are recovered [4].

Formulation of DES is the development of the Spalart-Allmaras turbulence model for RANS formulation [26], therefore the theoretical formulations are derived from the S-A model.

The S-A model uses modified turbulent viscosity $\tilde{\nu}$ in place of the turbulent kinematic viscosity.

$$\frac{\partial}{\partial t} (\rho \tilde{\nu}) + \frac{\partial}{\partial x_i} (\rho \tilde{\nu} u_i) = G_\nu + \frac{1}{\sigma_{\tilde{\nu}}} \left[\frac{\partial}{\partial t} \left\{ (\mu + \rho \tilde{\nu}) \frac{\partial \tilde{\nu}}{\partial x_j} \right\} + C_{b2} \rho \left(\frac{\partial \tilde{\nu}}{\partial x_j} \right)^2 \right] - Y_\nu + S_{\tilde{\nu}} \quad (3.47)$$

Turbulence production G_ν and destruction Y_ν terms are modeled as:

$$G_\nu = C_{b1} \rho \tilde{S} \tilde{\nu} \quad (3.48)$$

$$Y_\nu = C_{wq} \rho f_w \left(\frac{\tilde{\nu}}{d} \right)^2 \quad (3.49)$$

where d is the length scale calculated as the distance to the closest wall and \tilde{S} being the measure of deformation tensor:

$$\tilde{S} \equiv S + \frac{\tilde{\nu}}{\kappa^2 d^2} f_{v2} \quad (3.50)$$

where:

$$S \equiv |\Omega_{ij}| + C_{prod} \min(0, |S_{ij}| - |\Omega_{ij}|) \quad (3.51)$$

where:

$$C_{prod} = 2.0, \quad |\Omega_{ij}| \equiv \sqrt{2\Omega_{ij}\Omega_{ij}}, \quad |S_{ij}| \equiv \sqrt{2S_{ij}S_{ij}} \quad (3.52)$$

with the mean strain rate defined as:

$$S_{ij} = \frac{1}{2} \left(\frac{\partial u_j}{\partial x_i} + \frac{\partial u_i}{\partial x_j} \right) \quad (3.53)$$

The equation 3.49 shows that $\tilde{\nu}$ is proportional to the local deformation rate and wall distance: $\tilde{\nu} \propto Sd^2$. Smagorinsky model for "Sub-Grid-Scale" (SGS) scales the turbulent viscosity with local deformation and grid spacing: $\tilde{\nu} \propto S\Delta^2$.

By replacing the d in the S-A destruction term (eq. 3.49) with \tilde{d} :

$$\tilde{d} \equiv \min(d, C_{DES}\Delta) \quad (3.54)$$

a single model is obtained, acting as RANS with S-A turbulence modeling in regions where $d \ll \Delta$ and with LES behavior where $d \gg \Delta$. Grid spacing Δ is defined as the largest dimension of the computational cell $\Delta \equiv \max(\Delta x, \Delta y, \Delta z)$. In case of an ambiguous grid definition, where $\Delta < \delta$ the DES limiter can activate the LES mode inside the boundary layer, where the grid is not fine enough to sustain resolved turbulence. Therefore, a new formulation [25] of DES is available to preserve the RANS mode throughout the boundary layer. This is known as the delayed option or DDES for delayed DES [4].

DES and DDES methods can be used with other RANS turbulence models. Further analyses presented in this thesis use a $k - \omega SST$ model. For hybrid model the dissipation of turbulent kinetic energy is modified:

$$Y_k = \rho \beta^* k \omega F_{DES} \quad (3.55)$$

where:

$$F_{DES} = \max \left(\frac{L_t}{C_{DES} \Delta_{max}} (1 - F_{SST}), 1 \right) \quad (3.56)$$

where C_{DES} is a calibration constant used in the DES model and has a value of 0.61, with $F_{SST} = 0, F_1, F_2$ where F_1 and F_2 are the blending functions of the Baseline and $k - \omega SST$ model. The turbulent length scale is the parameter that defines this RANS model:

$$F_{DES} = \max \left(\frac{L_t}{C_{DES} \Delta_{max}}, 1 \right) \quad (3.57)$$

The F_{DDES} blending function is given by equation 3.57 with model constants $C_{d1} = 20$, $C_{d2} = 3$ and r_d as defined by eq. 3.59:

$$F_{DDES} = \tanh \left[(C_{d1} r_{d1})^{C_{d2}} \right] \quad (3.58)$$

$$r_d = \frac{\nu_t + \nu}{\kappa^2 y^2 \sqrt{0.5 (S^2 + \Omega^2)}} \quad (3.59)$$

3.3 Mesh sizing requirements

Let's assume a sinusoidal pressure fluctuation $y(t)$ (eq. 3.60) of ordinary frequency of f and amplitude A , moving through ambient medium for more than 5 cycles at speed of sound (eq. 3.61). The mathematical and numerical methods for solving flow field

described in section above are capable of computing such pressure fluctuation in a computational mesh of relevant resolution.

$$y(t) = A \sin(2\pi ft + \phi) \quad (3.60)$$

$$a = \sqrt{\kappa RT} \quad (3.61)$$

Cell size and time step size are limited by the wave length, and therefore frequency of the discussed pressure fluctuation. The wavelength is calculated by formula 3.62.

$$\lambda = \frac{v}{f} \quad (3.62)$$

Considered fluctuation travels through the finite volumes (that is: CFD mesh cells) in the stationary CFD mesh. Pressure value is measured at the cell centroid for each timestep. At this stage, it is assumed that timestep is of relevant resolution for the analysis, the mesh is isotropic in x , y and z directions and that the propagation has only one directional component. Four possibilities are considered.

Scenario 1: wavelength is smaller than the edge length of the cell in the direction of propagation. In this condition, the pressure fluctuation performs a number of cycles within one cell (Fig. 3.2). Due to the numerical approach, such fluctuation will be filtered out.



FIGURE 3.2: Scenario 1. Wavelength smaller than cell edge length

Scenario 2: wavelength and cell edge length in the direction of propagation are equal. In this condition, the pressure fluctuation performs one cycle within one cell in the direction of the fluctuation propagation (Fig. 3.3). Such pressure change will be also filtered out by the numerical scheme.

Scenario 3: wavelength is equal to 4 cell edge lengths. This is the minimum cell size condition for proposed approach. In this condition, the pressure fluctuation performs one cycle within four cells in the direction of the fluctuation propagation (Fig. 3.4). FVM



FIGURE 3.3: Scenario 2. Wavelength equal to cell edge length

method is now capable of computing the pressure fluctuations resulting from sound wave propagation.



FIGURE 3.4: Scenario 3. Wavelength equal four minimum edge lengths

Scenario 4: wavelength is larger than 4 cell edge lengths. In this condition, the pressure fluctuation performs one cycle within multiple cells in the direction of the fluctuation propagation (Fig. 3.5). FVM method computes pressure from the sound wave propagation across multiple cells.



FIGURE 3.5: Scenario 4. Wavelength larger than four minimum edge lengths

Based on these possibilities, the edge sizing of the finite volume cell should be at least four times smaller than the shortest wavelength expected in the flowfield.

3.4 Timestep requirements

There are two limiting factors for timestep requirements. The high frequency signal is limited by the timestep size, whereas the low frequencies are limited to the total number of timesteps and physical flow time calculated. The timestep size is calculated first.

Once mesh cell sizing is established, time at which the fluctuation passes the cell is established by simple formula 3.63. Distance s is the cell edge sizing, obtained as in section 3.3 and the relation between cell size and wavelength is presented in equation 3.65.

$$a = \frac{s}{t} \quad (3.63)$$

where

$$t = \frac{1}{f} \quad (3.64)$$

$$s = \frac{\lambda}{4} \quad (3.65)$$

By rearranging the equation 3.63 to solve for t and substituting λ by 3.62 we obtain:

$$t = \frac{s}{a} = \frac{\lambda}{4a} = \frac{a}{f} \cdot \frac{1}{4a} = \frac{1}{4f} \quad (3.66)$$

Time step t must comply with the requirements of the FFT analysis occurring further in the process as it becomes the minimum sampling time for the sound pressure signal. Therefore it must be compared with the requirements stated by Shannon-Nyquist-Whitaker theorem: *If a function $x(t)$ contains no frequencies higher than B hertz, it is completely determined by giving its ordinates at a series of points spaced $1/(2B)$ seconds apart.*

Equation 3.66 shows that time step for the analysis is dependent from the expected value of high frequency fluctuations.

In order to capture frequencies on the low end of the spectrum, the analysis must be performed long enough to capture at least a single, with optimum 5 or more fluctuations of the desired low frequency. Assuming lower end of the audible frequency spectrum, the 20Hz frequency, the simulation time must resemble at least 0.05s of flowtime with optimum 0.25s of flowtime at given timestep.

3.5 Limiting factors of the direct approach

Described direct formulation noise analysis is solely a post processing approach relying on data generated on CFD analysis. In order to obtain reasonable results down the process, the analysis itself must be capable of delivering pressure fluctuations that can be considered as acoustic in source.

It is advised to use a turbulence model that is capable of resolving small scale turbulence on a mesh that will allow such resolution. Utilizing LES formulation or at least hybrid RANS/LES turbulence model such as DDES. Using an averaging formulation such as RANS will cut off all of the fluctuations and is not suitable for this approach.

The range of frequencies captured by this method depends on the mesh sizing and timestep sizing. Therefore, if the range of expected frequencies is known or at least estimated, the mesh sizing and timestep size can be adjusted for the given case. For analysis within audible range, 4000 timesteps are required for one 20Hz period. Considering the mesh sizing requirements, the mesh cell count will rise up to tens of millions for a single passage axial compressor blade. This makes the case files and storing data for each timestep relatively challenging and requires securing adequate storage beforehand.

A major limiting factor is the implementation of the direct noise formulation post-processing. For this thesis, the method was implemented in python v.3.5 high level programming language. Python code is written in C/C++ and provides a vast array of additional libraries for handling files, tabular data and performing mathematical operations. The code is presented in appendices to this dissertation. Although easy to implement, python code is known to be inefficient and slow while managing large amounts of data. Tools and algorithms used in implementing the averaging, obtaining sound pressure and particle velocity as well as DFT are built in tools from specific libraries. As convenient for the implementation, the post-processing code requires some amount of operational memory and disk space for generating the results.

The programming language used for the post-processing of data must be capable of generating 2D and 3D plots for visualization purposes. Ideally the processed and visualized data should resemble the mesh from which the initial data was gathered.

Chapter 4

Test case

4.1 NASA Rotor 67 transonic axial compressor

The direct approach noise analysis is conducted on a NASA Rotor 67 (R67) transonic axial compressor. Originating as a first stage of two stage fan for evaluation of design procedures, validation of experimental facilities as well as meshing and CFD tools. The test case was used in a multitude of studies for turbomachinery aerodynamics, geometry optimisation, noise analyses and structural analyses. Full design procedure can be found in references [12] and [29]. The CFD analysis and direct approach noise analysis is performed on a single passage of a first stage rotor of the compressor. The setup for the calculations (apart from the single passage constraint) is relevant to a case described in study [27], which was the main source for geometry and flowfield data.

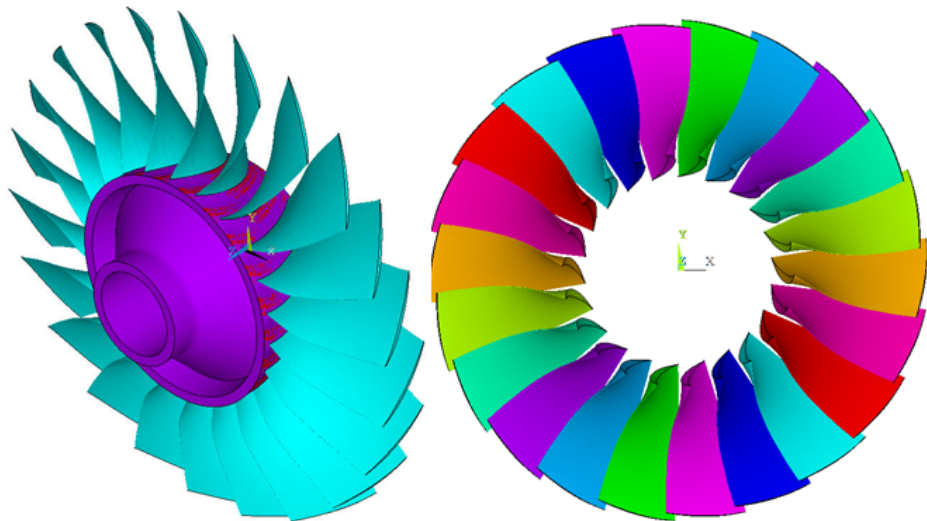


FIGURE 4.1: Geometry of NASA R67

Basic parameters of the given rotor are, design pressure ratio of 1.63 at massflow of 33.25 kg/sec. The design rotational speed is 16 043 rpm, which yields a tip speed of 429 m/s and an inlet tip relative Mach number of 1.38. The rotor has 22 blades and an aspect ratio of 1.56 (based on average span/root axial chord). The inlet and exit tip diameters are 514 and 485 mm, respectively, and the inlet and exit hub/tip radius ratios are 0.375 and 0.478, respectively. A fillet radius of 1.78 mm is used at the airfoil-hub juncture. The square root of the mean square of the airfoil surface finish is 0.8 μm or better, the airfoil surface tolerance is ± 0.04 mm, and the running tip clearance is approximately 1.0 mm [27]. Surface roughness and some of the geometrical features are omitted during the preparation of the geometry and CFD mesh for reasons described in sections 4.2 and 4.3. General geometry of NASA R67 is presented on fig 4.1. Basic parameters of the test subject are presented in table 4.1

TABLE 4.1: Basic R67 parameters

Parameter	Value	Unit
Π	1.63	-
\dot{m}	33.25	kg/s
ω	16043	rpm
v_t	429	m/s
Ma_t	1.38	-
blade count	22	-

4.2 3D geometry preparation

References [12] and [29] provide the blade geometry for both stages of the compressor as a Multiple-Circular-Arc definition. In the MCA approach the design blade elements lie on conical surfaces which approximate the actual stream flow surfaces. More specifically, the mean camber line and the suction and pressure surface lines of a blade element are lines with a constant rate of angle change with path distance on a specified conical surface [11]. Although relatively comfortable for design purposes, such approach requires transforming the MCA blade to Cartesian or cylindrical coordinates. Reference [11] provides an extended definition of MCA blade description as well as Fortran code for generating blade cross-section and computing geometric properties of the blade.

Source [27] provides a list of coordinates for 14 profiles of the 1st stage rotor blade suction and pressure surface, as well as coordinates for hub and casing path in the meridional plane. These coordinates were used to create the geometry of the single passage of the subject blade. Cartesian coordinates are also available in Appendix ?? and project Github repository [21].

The coordinate system is a standard right-hand Cartesian CS. Rotation axis is set to Z-axis with flow in positive Z direction. The compressor rotation is set as in right-hand rule, the compressor rotates in clockwise direction when viewing the blade leading edge. Z = 0 coordinate is defined by point number 1 on 1st blade design surface.

Hub and casing flow paths were created by importing formatted point data as a b-spline curve, followed by extrusion the curve to surface by rotating it by $\pm 60^\circ$. Suction and pressure surface of the blade were created by importing the cartesian coordinates if the design airfoils and creating a lofted surface along the imported splines. Leading and trailing edge radii were created in a similar manner, with use of edge radius and edge tangency points given in original study [27]. Tip gap of the blade was created by offsetting the casing surface by 1.016 mm in the normal direction towards the rotation axis and creating a section line between blade surfaces and the offset surface.

Due to the estimated mesh cell count, only one blade passage is created, therefore a set of periodic surfaces must be defined. ICEM software is capable of creating a midline as an average of coordinates of two given lines. A midline was created for every design profile and was manually extended beyond the blade leading and trailing edge. Midlines were lofted to create a midsurface which was later on copied with rotation by $\pm 0.5 \cdot \frac{360^\circ}{22}$ to create two identical periodic surfaces.

Aforementioned midlines were also rotated along Z-axis to create control surfaces for mesh stabilization and data acquisition down the process.

Reference [27] provides coordinates of hub and casing for the full experiment, however only a rotating part of the experimental rotor setup is be used. Two surfaces normal to Z direction at coordinates Z = -13.74 mm and Z = 93.65 mm are placed as inlet and outlet boundary conditions. Geometry was finished by necessary extrusions, trimming and other finishing operations to ensure high quality surface for meshing.

Physical experiment test compressor has a 1.78 mm fillet at airfoil-hub juncture. This feature was omitted as it would unnecessarily complicate the meshing process and increase the cell count.

Such approach allowed for creating a geometry for single blade passage with centered blade of 1st stage rotor of the test compressor (Fig 4.2).

4.3 Meshing approach

Following requirements are posed to the mesh for the discussed case:

- Possibly low number of elements fulfilling the mesh sizing requirements stated in chapter 3.1,

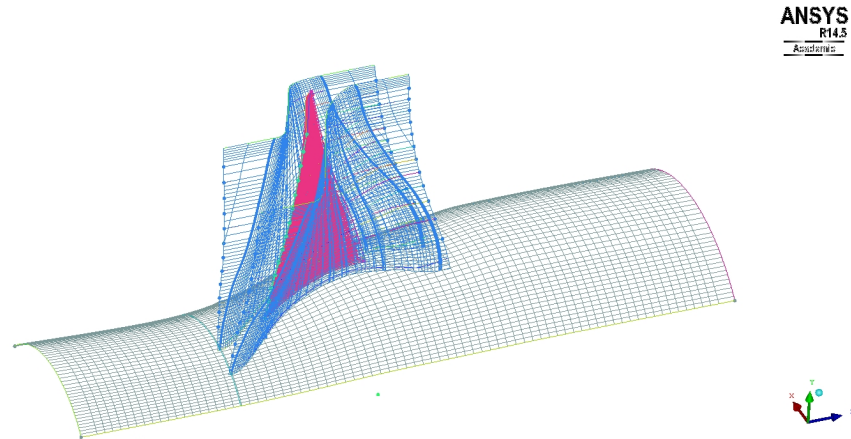


FIGURE 4.2: Final single passage geometry. Some features hidden for clarity

- Mesh should be a fully structural mesh including the tip gap,
- The periodic boundary mesh must be identical/conforming for both boundaries,
- The mesh must have high quality metrics in terms of cell orthogonality and skew as defined by equations 4.1 & 4.2 respectively.

$$\text{Orthogonality} = \frac{\vec{A}_i \cdot \vec{f}_i}{|\vec{A}_i| \cdot |\vec{f}_i|} \quad (4.1)$$

$$\text{Skewness} = \frac{\text{Optimal Cell Size} - \text{Cell Size}}{\text{Optimal Cell Size}} \quad (4.2)$$

One of the initial mesh concepts was an unstructured mesh with triangular surface mesh extruded to prism boundary layer and mostly isotropic tetrahedra in the volume. This approach was quickly rejected for bad quality elements near the airfoil/hub junction and tip gap, as well as element count in range of 4.5 million cells for sizing relevant for RANS analysis. This approach was quickly dropped.

A non-trivial topology with fully conforming periodic boundaries was introduced (fig 4.3). The topology creates a high quality mesh, yet it is impossible to apply a structural tip gap due to non-conforming element count on the pressure and suction side of the mesh. A RANS sufficient mesh without tip gap area (blade was extended to the casing surface) was created. The cell count for this mesh is below 0.5 million cells with better skewness and orthogonal quality. This mesh was utilized for initial numerical setup and data acquisition testing.

Final topology was a standard h-grid topology for generic airfoils (fig. 4.4). Although it is impossible to create a conforming periodic interface with such mesh topology, a fully

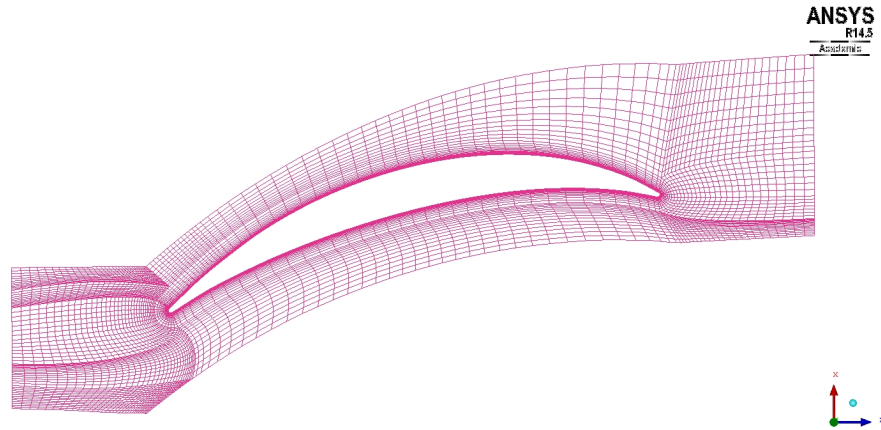


FIGURE 4.3: Mesh topology with conforming periodic boundaries

structural tip gap was implemented. Omitting the blade-hub juncture fillet simplified the mesh. Such topology eradicates the necessity of placing 5-way topology points.

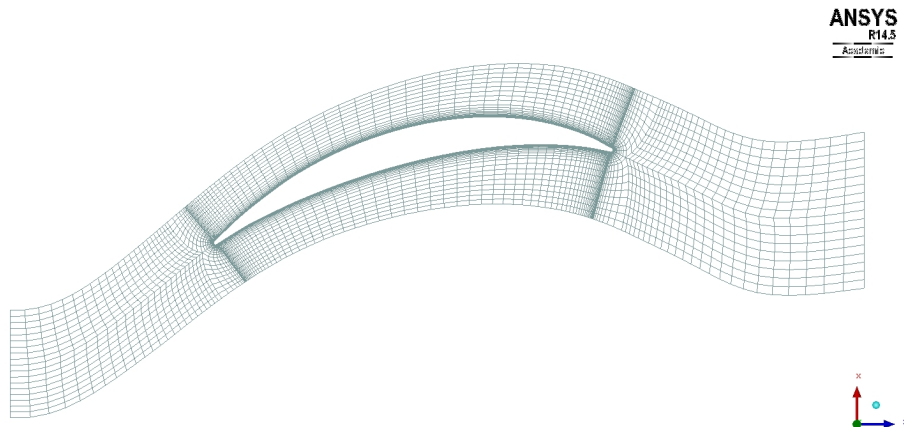


FIGURE 4.4: Mesh h-topology

As there were no information about the frequency of the pressure fluctuations at time of creating the mesh, the analysis will focus on the audible range of sound frequencies from 20Hz to 20 000Hz. The wavelengths for given frequencies are calculated by formula 3.62 and divided by four to obtain the required cell sizing. The velocity of sound obtained by equation 3.61 with reference temperature $T = 300K$. The results are presented in table 4.2.

TABLE 4.2: Test case boundary conditions

Frequency [Hz]	Wave length [m]	Cell size [m]
20	17.390	4.347
20 000	0.01739	0.004347

Maximum element edge length is limited to 3 mm, with 5 mm at inlet and outlet boundary conditions. The mesh cell sizing requirements are described in chapter 3. Blade boundary layer is produced by creating an o-grid around blade surface mesh. Hub and casing boundary layers are created by changing the sizing on the blocks adjacent to respective surface mesh. Sizing of the first element is estimated with y^+ parameter as described in equation: 4.3. First element thickness in on the blade surfaces ranges from is $2\mu m$ on tip airfoil and $10\mu m$ on hub airfoil. This corresponds to $y^+ \approx 2$ calculated by streamline velocity values given in experimental study [27].

$$\Delta s = \frac{y^+ \mu}{U_{fric} \rho} \quad (4.3)$$

where:

$$U_{fric} = \sqrt{\frac{\tau_{wall}}{\rho}} \quad (4.4)$$

where:

$$\tau_{wall} = \frac{C_f \rho U_\infty^2}{2} \quad (4.5)$$

where:

$$C_f = \frac{0.026}{Re_x^{1/7}} \quad (4.6)$$

Internal volume of the mesh was stabilized by attaching the mesh blocks to the internal design surfaces, which represent the design streamline surfaces of the experimental rotor. This ensures that mesh layers are mostly coincident with the primary flow streamlines. The internal surface mesh is also used for data acquisition purposes. The markers are named hub, int-01 thru int-12 and int-tip corresponding to following locations of the design surfaces. The span percentage is calculated from the hub.

TABLE 4.3: Location of compressor desing surfaces

Boundary marker	Location
hub	0% span
int-01 - int-12	7.7% - 92.3% every 7.7% span
int-tip	100% span

Figure 4.5 provides overview of mesh quality defined by equations 4.1 and 4.2. The quality of created mesh is sufficient for both RANS and DDES analyses (chapter 5). Final mesh reached c.a. 11.5 million cell count. Final mesh is presented in figure 4.6

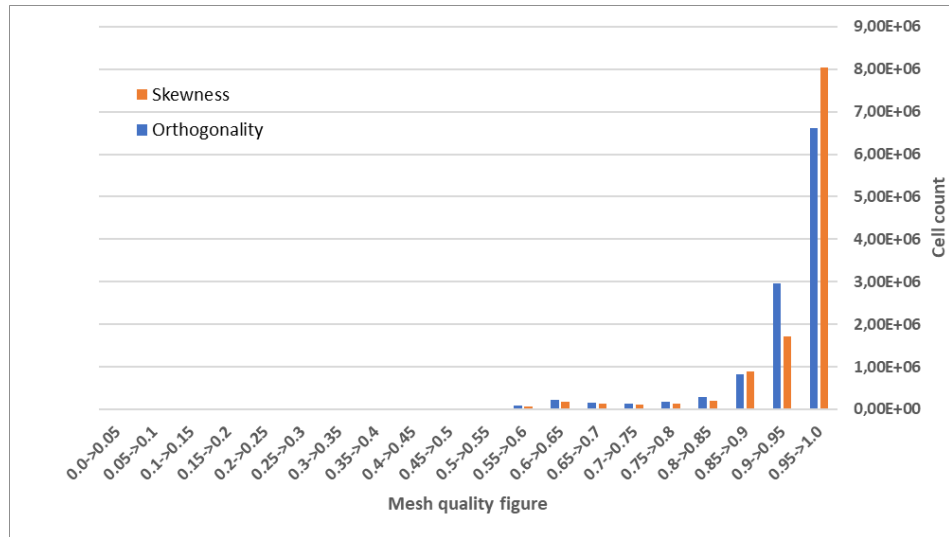


FIGURE 4.5: Mesh quality histogram

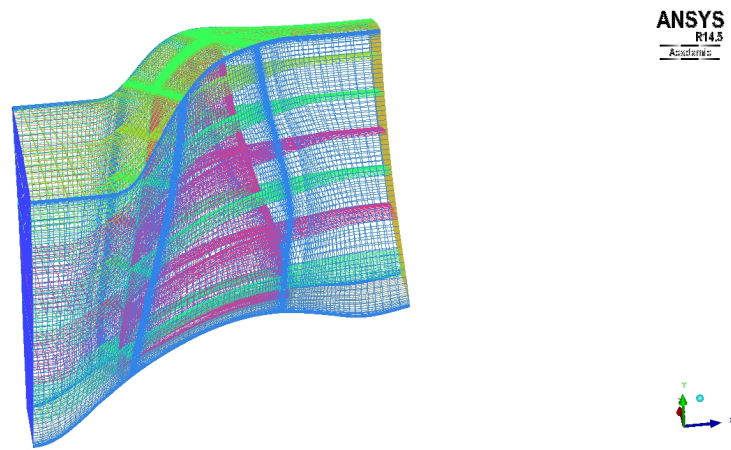


FIGURE 4.6: Completed Mesh

Chapter 5

CFD Analysis

5.1 Case preprocessing

CFD analyses for generating raw pressure field data are performed in ANSYS Fluent 17.2 software on Prometheus HPC cluster located in Kraków. Access for this infrastructure was granted by PLGrid infrastructure. Calculations were run on 5 nodes of 24CPU cores and 128GB RAM each [5], which resulted in decomposition to 120 cores, resulting in allocating around 110 thousand cells to a single CPU core.

The analysis is set to "peak efficiency" conditions of the experimental test case. Apart from the turbulence modeling approach, the set up is consistent throughout the CFD cases.

Material used in the analysis resembles standard air modeled as ideal gas as in equation with following properties described in table 5.1

TABLE 5.1: Standard air properties

C_p	1006.43	J/(kg · K)
λ	0.0242	W/(m · K)
μ	$1.7894 \cdot 10^{-5}$	kg/(m · s)
M	28.966	kg/kmol

$$pV = nRT \quad (5.1)$$

Analysis operating pressure is set to 0 Pascal, which is a standard practice in compressible flow CFD. Internal mesh zone is set as "frozen rotor" reference frame. Although no mesh motion is implied, the effect of Coriolis accelerations and centrifugal acceleration will be taken into account by adding respective acceleration components to momentum equations as described in chapter 3. The rotational velocity is set to 1680 rad/s.

Following boundary conditions were applied. The setup is typical for compressible flow CFD cases performed in the authors institute.

TABLE 5.2: Test case boundary conditions

Boundary marker	Boundary type			
Inlet	Pressure Inlet	101350	Pa	
Outlet	Pressure Outlet	102000	Pa	
Hub	Moving wall	1680	rad/s	
Blade	Moving wall	1680	rad/s	
Casing	Stationary wall			
Internal profiles	Internal			
Periodic boundaries	Interface			

5.2 Flowfield initialization & RANS

RANS analysis is not suitable for generating acoustic nearfield data as the method averages the fluctuations over time (chapter 3). Yet, this approach is used to solve the initial flowfield at a relatively low computational effort. Furthermore the RANS analysis provides initial validation results of the model setup and solver settings.

The solver is set up to steady-state, density based, coupled-implicit solver with $k - \omega$ SST turbulence model. Such setup is a go-to setup for nearly all compressible aerodynamics CFD done in the author's institute.

The density-based solver in ANSYS Fluent solves the governing equations of continuity, momentum, and (where appropriate) energy and species transport simultaneously as a set, or vector, of equations. Governing equations for additional scalars will be solved sequentially (that is, segregated from one another and from the coupled set). Two algorithms are available for solving the coupled set of equations, the coupled-explicit formulation and the coupled-implicit formulation [4].

The system of governing equations for a single-component fluid, written to describe the mean flow properties, is cast in integral Cartesian form for an arbitrary control volume V with differential surface area dA as follows:

$$\frac{\partial}{\partial t} \int_V W dV + \oint_V [F - G] \cdot dA = \int_V H dV \quad (5.2)$$

where:

$$W = \begin{bmatrix} \rho \\ \rho u \\ \rho v \\ \rho w \\ \rho E \end{bmatrix} \quad F = \begin{bmatrix} \rho v \\ \rho uv + pi \\ \rho vv + pj \\ \rho ww + pk \\ \rho vE + pv \end{bmatrix} \quad G = \begin{bmatrix} 0 \\ \tau_{xi} \\ \tau_{yi} \\ \tau_{zi} \\ \tau_{ij}v_j + q \end{bmatrix} \quad (5.3)$$

and where the vector H is the body forces and energy source vector.

The ρ, v, E, p are respectively the density, velocity, total energy per unit mass and pressure of the fluid. τ is the viscous stress tensor and q is the heat flux.

Total energy E and total enthalpy H are related by the formulas:

$$E = H - \frac{p}{\rho} \quad (5.4)$$

$$H = h + \frac{|v|^2}{2} \quad (5.5)$$

Equation 5.2 is preconditioned, convective fluxes are splitted with Roe Flux-Difference Scheme and the preconditioned equation is discretized with Euler Implicit discretization and combined with Newton type linearization of fluxes. Obtained equation system is solved by the Incomplete Lower Upper (ILU) factorization in conjunction with the Algebraic-Multi-Grid. Details on the solver theory used in this study are available in source [4]

Flowfield is initialized at first with constant values populated from the "inlet" boundary condition patch. Next a Full-Multi-Grid initialization is performed to generate coarsened flowfield. The analysis is then processed by first, second and third order discretization schemes for all of the conservation values, up to a given residual value. It must be noted, that for second and third order scheme analyses, convergence criteria may not be reached. Should this case occur, the analysis is stopped once the residual plots reach a plateau and the resulting flowfield is considered acceptable. Once the third order scheme analysis is completed, data is acquired from inlet and outlet boundary conditions, and the constant pitch vs. span streamlines.

The analysis is set to a moderately strict residual convergence criteria of 10^{-6} , however is monitored during runtime. Once the convergence plot reaches plateau and the internal surfaces flow field is not changing throughout iterations the analysis is stopped and switched to a higher discretization scheme or finalized and saved.

5.3 DDES analysis

Once the RANS analysis is converged to a satisfactory level the setup is changed to a transient, pressure-based, PISO scheme solver with DDES turbulence model and $k - \omega SST$ RANS formulation for shielded regions and subgrid scale. Rationale for the DDES analysis is provided in chapter 3. Pressure based solver is required by the DDES implementation in the used software. Utilization of the pressure based solvers for compressible flows is known to be unstable during the calculations, especially for the adverse pressure gradient cases. However, once the initial flow field resembles the final flowfield, the pressure based calculations are rather stable even at high velocity adverse pressure gradients.

Pressure based solver solves the discretized continuity equation with obtaining the velocity field from the momentum equations. The pressure field is obtained by solving and manipulating the continuity and momentum equations within a pressure velocity coupling scheme.

Transformed and discretized equations are solved by a linear solver and the intermittent solutions are coupled using a pressure velocity coupling algorithm. For this specific case PISO scheme is chosen for the computation. The algorithm is suitable for calculating problems with larger (in comparison to density-based acoustical timescale) pseudo-timestep and with decreased computational expense. Figure 5.1 presents the flow of the PISO algorithm.

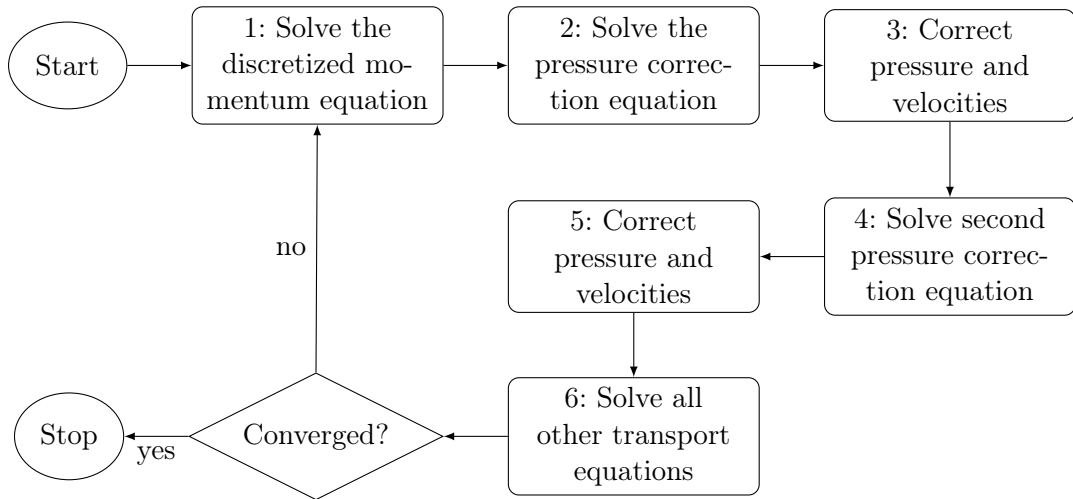


FIGURE 5.1: Flowchart of the PISO algorithm

As the flowfield resulting from the RANS analysis is averaged over time and has no distinguishable features of a turbulent flow, the DDES analysis is divided into two runs. The first run is set to create a flowfield with random flow features. This is also used for testing the convergence and data acquisition process.

Although not required by the "frozen-rotor" configuration, the timestepping is based on the rotor Blade-Pass-Frequency number. The BPF parameter is obtained by formula 5.6

$$BPF = \frac{n \cdot t}{60} \quad (5.6)$$

where t is the number of blades and n is the rotational speed in rpm.

For NASA R67 the base Blade Passing Frequency is equal to 5882.36Hz . By multiplying the BPF by four a frequency of 23529.44Hz is obtained. The frequency is above the human audible range and will be used to compute the timestep. As stated in chapter 3, in order to capture a given frequency, the timestep must be at least 4 times smaller than the period of the oscillations (equation 3.66). By this approach the maximum timestep of the DDES calculation is $1.06 \cdot 10^{-5}\text{s}$. The timestep is compared with the requirements of the Courant-Friedrichs-Levy condition defined by equation 5.7

$$Co = \frac{u \cdot \Delta t}{\Delta x} \quad (5.7)$$

Considering that $u_{max} = 426.72\text{m/s}$ and $\Delta x = 0.25 \cdot \lambda = 0.003695\text{m}$ for desired frequency of 23529.44Hz and timestep of $1.06 \cdot 10^{-5}\text{s}$ the Courant number obtained is equal to 1.22. By rearranging the equation to solve for Δt an equation 5.8 is obtained and a calculation timestep fulfilling requirements of the CFD analysis and the direct noise formulation is computed and is equal to $8.659 \cdot 10^{-6}$.

$$\Delta t = \frac{Co \cdot \frac{\lambda}{4}}{u_{max}} \quad (5.8)$$

Initial timestep for the DDES analysis is set up to $5.0 \cdot 10^{-6}\text{s}$. Presented time stepping approach fulfills the Shannon-Nyquist-Whitaker theorem presented in section 3.4. First run was conducted for c.a. 30 thousand timesteps, during which following factors were tested: calculation efficiency dependent on the CPU core count used, data output and data format, estimated storage requirements and the output from the embedded FW-H aeroacoustical models. First run concluded, that the assumed timestep does not meet the required convergence criteria and delivered inaccurate results or flowfield with features not resembling the features characteristic for compressor flow.

The timestep was gradually decreased to a value of $1.0 \cdot 10^{-6}\text{s}$, the CPU core count was set to 120 CPU cores distributed over 5 HPC nodes. Once the first run produced a fully developed flowfield with turbulent features characteristic to the LES analysis, the case was saved and set up for a final run with full data acquisition.

It was desired to capture at least 0.05 seconds of the flow but with some relation to geometric and operational features of the rotor. Based on the blade count and rotational speed of the rotor a time of a single periodic passage is calculated to $1.70 \cdot 10^{-4} s$. Next the required computational time is divided by the passage time to obtain the number of blade passages. 294.118 passages will occur during the 0.05s, so the number is rounded up to 295 passages and multiplied again by the passage time. Total calculation time of 0.05015 seconds is obtained. Therefore 50150 timesteps is required for full calculation runtime, with one passage being calculated in 170 timesteps.

5.4 Validation of the results

The experimental study [27] provides a very extensive set of validation data for the passage flowfield. The quoted study presents results of LDA measurements of the NASA R67 compressor for relative mach number and relative flow angle at constant pitch and constant chord lines intersecting with blade span lines at 10% intervals. Constant pitch line is derived from the blade's suction surface: 0% percent pitch is the suction surface of one blade, 100% pitch is the suction surface of the adjacent blade. Constant chord lines are used to plot blade-to-blade distributions of given parameters at intersection of span and constant z-coordinate surface (fig. 5.2).

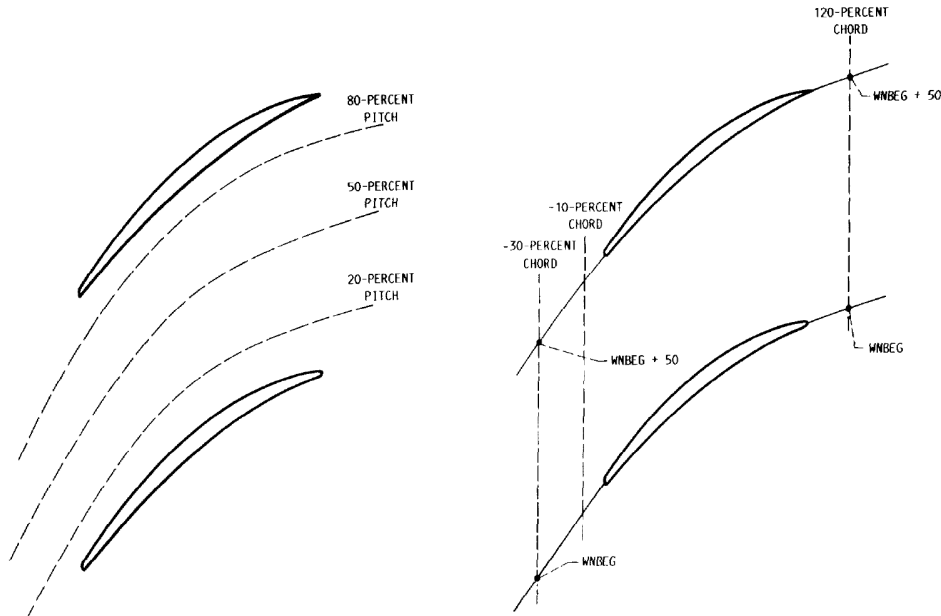


FIGURE 5.2: Constant pitch (left) and constant chord (right) lines [27]

In order to validate the CFD analysis, the constant pitch surfaces for 20%, 50% and 80% constant pitch are combined with 10%, 50% and 90% constant span locations, as measured from the blade tip, thus producing 9 lines to for relative Mach number and

relative flow angle data. Furthermore, Mach contour plots for 10%, 30% and 70% constant span surfaces (measuring from the blade tip) are compared with the experimental study.

For clarity, relative mach number plots and constant pitch plots are presented in appendix ??.

The most simple method for validating the results is comparing the total and static pressure values on inlet and outlet boundary conditions of the domain with experimental data. Plots for static and total pressure at inlets and outlets of the domain are presented in figures 5.3 and 5.4.

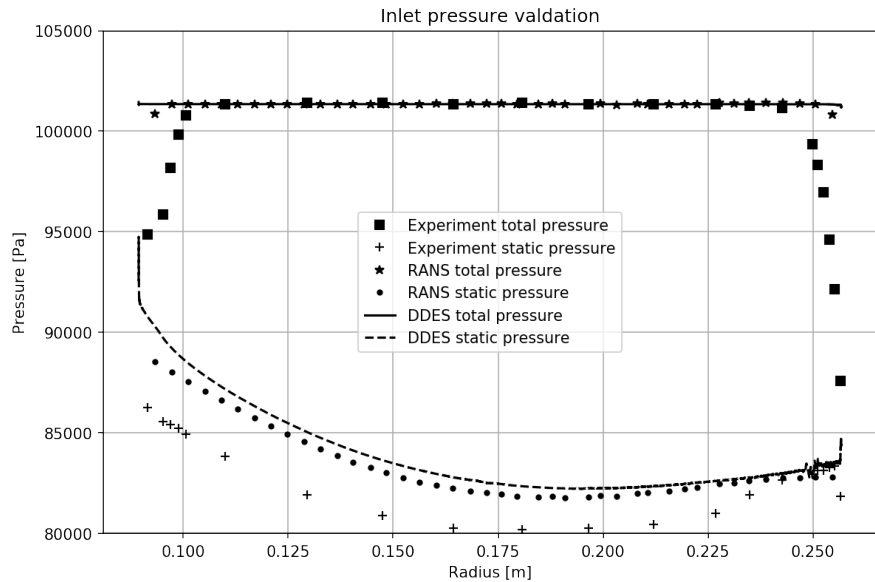


FIGURE 5.3: Inlet pressure validation

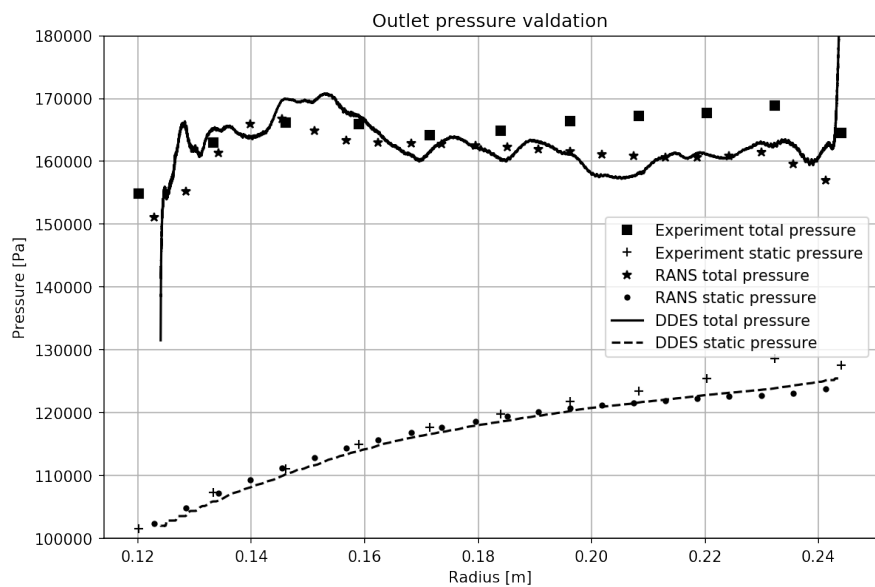


FIGURE 5.4: Outlet pressure validation

Both RANS and DDES analyses produce results that are confirmed by the experimental data. Static inlet pressure plot show the discrepancy between experimental and CFD data resulting from a minor shift between the inlet and outlet CFD boundaries and the location of the pressure rake. The inlet boundary condition is moved closer towards the leading edge of the rotor, than the experimental pressure measurements array, therefore the static pressure is increased. The Mach number contour plots on the corresponding internal surfaces show the same character of the flow. Discrepancies between the experimental study and the obtained CFD results arise from a slight offset between the experimental surfaces as the mesh internal surfaces.

Chapter 6

Results of flow field noise analysis

6.1 Transition from flow-field to sound signal data

The performed DDES analysis delivered a set of files for further postprocessing. Values of static pressure, velocity magnitude, vorticity magnitude, static density and static temperature were gathered from designated boundaries and internal surfaces representing the design streamline cones. The dataset consists of 50150 files for each of the 13 internal surfaces and 5 blade boundaries, resulting in over 5.5 TB of data.

This set was postprocessed to obtain the sound pressure, sound intensity and their respective decibel values for each timestep. The mathematical formulas for obtaining these values are provided in chapter 3 and the Python 3.5x implementation of which is presented in appendix ???. The postprocessing of flow field data to sound data was performed on the same HPC infrastructure as the DDES analysis, due to the file accessibility. Postprocessed dataset was saved in a folder structure resembling the source files.

6.2 Sound levels results

6.2.1 Results postprocessing

The time specific sound pressure values were further processed to obtain the Root Mean Square values of sound pressure and sound intensity from internal markers and blade surfaces. Due to large number of figures, the scatter plots of the aforementioned values are provided in the Appendix ?? in figures ?? thru ???. Providing data for both pressure and intensity values and their decibel levels is redundant, yet both plots are shown for clarity and direct comparison of given values.

Internal boundary plots provide information on maximum and minimum values of SPL and SPLdB presented on the plot. As the minimum sound intensity (SIL) is equal 0 and the SILdB values for corresponding points approach negative infinity. Such values were overridden to show 0 SILdB on the plot. For this reason minimum value coordinates are omitted in the plot description.

Sound pressure and intensity plots are scaled with a normalized logarithmic colorbar with common scale across all of the internal surface and blade surface plots. For sound pressure, the maximum obtained value is 13917.395 Pa , therefore the maximum value of the plot scale is liberally rounded up to 15000 Pa . Minimum value for SPL is in range of 10 Pa , so the lower bar limit is set to zero. As for the Decibel values the lowest obtained value is around 116 dB , largest - around 177 dB . The plot scale is therefore set to $100 - 180 \text{ dB}$ range with linear scale. The same approach was used for maximum values of sound intensity. For sound intensity itself, the colorbar was limited from 0 W/m^2 to $1.2 \cdot 10^6 \text{ W/m}^2$ and normalized to logarithmic scale. For SILdB plot, the bar range is limited to 0 dB to 180 dB range with linear scale.

Plots are created by projecting points from 3D surface onto a 2D canvas of the plot, therefore some shape aberrations may occur. Color of the point is normalized as described above. Plot axis labels correspond with the global coordinate system of the geometry.

6.2.2 Qualitative analysis

Averaged sound pressure and sound intensity plots provide some information on the character of the acoustic phenomena modeled in a stationary reference frame for given test compressor.

The sound pressure fluctuations that translate to high SPLdB values occur in regions where flow is turbulent. For internal control surfaces, where flow is globally subsonic (int-01, int-02, int-03 – figures ?? thru ??), the sources of the aerodynamically induced noise correspond to the regions on flow separation on the suction surface (upper on the plots). This is especially visible in the wake of the blade. Figures ?? and ?? provide the view of the blade's suction surface. A separation of the flow at leading-edge-to-hub transition leading to a very characteristic secondary flow and corner stall separation (separated flow on the suction surface near the trailing-edge-to-hub transition). The largest pressure fluctuations were noted on the trailing edge and trailing-edge-to-tip transition, which is visible on both blade surface plots and internal surfaces plots.

Internal surface contour plots show, that the source of sound pressure is the supersonic-to-subsonic transition occurring on the shockwave. The effect of shock induced flow separation is becoming visible on internal surface plots for surfaces int-04 and int-05 (figures ?? thru ??), with full visibility of described phenomena on surfaces int-06 thru int-12

(figures ?? thru ??). Plot for surface adjacent to the blade tip (surface int-tip, figures ?? thru ??) show the effect of "tip-leakage" phenomena when high pressure flow at the pressure side of the compressor creeps to the low pressure suction side thru the tip gap (Fig. 6.1).

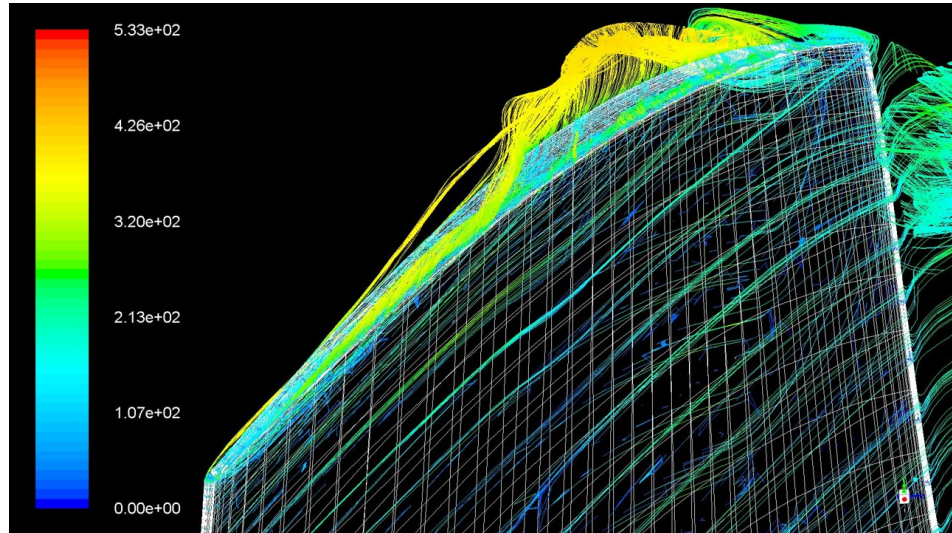


FIGURE 6.1: Tip gap streamlines. Velocity in [m/s]

Presented contour plots show a rather significant noise level in the supersonic (relative to the blade) region along with patterns resembling sound waves. SPLdB noise level in lower range of 120 decibels corresponds to pressure fluctuations in range of 20 Pa in medium where average static pressure is in range of $0.8 \cdot 10^5 \text{ Pa}$, which may result from typical for transient calculations pressure fluctuations.

Sound wave like patterns on blade suction surface in the supersonic region require further investigation. Wave like pattern presented on the RMS plot is likely to show a sort of standing wave pattern evolving towards the leading edge of the blade. Region of flow for containing this phenomena is supersonic relatively to the blade, however both axial and radial components of the flow are subsonic. Moreover, the boundary layer flow for this case is subsonic even in the relative supersonic region, therefore sound propagation is possible near the blade surface.

6.2.3 Quantitative analysis

Morbi rutrum odio eget arcu adipiscing sodales. Aenean et purus a est pulvinar pellentesque. Cras in elit neque, quis varius elit. Phasellus fringilla, nibh eu tempus 1venenatis, dolor elit posuere quam, quis adipiscing urna leo nec orci. Sed nec nulla auctor odio aliquet consequat. Ut nec nulla in ante ullamcorper aliquam at sed dolor. Phasellus fermentum magna in augue gravida cursus. Cras sed pretium lorem. Pellentesque eget

ornare odio. Proin accumsan, massa viverra cursus pharetra, ipsum nisi lobortis velit, a malesuada dolor lorem eu neque.

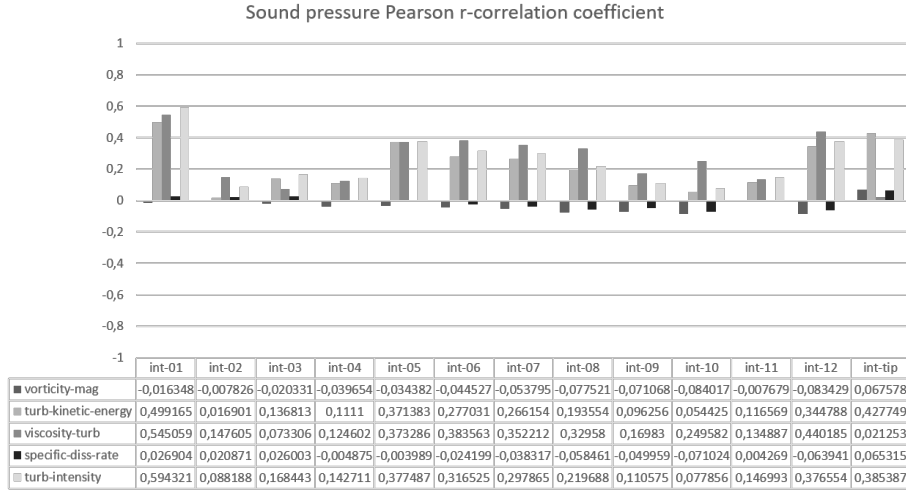


FIGURE 6.2: SPL to flowfield turbulence values correlation

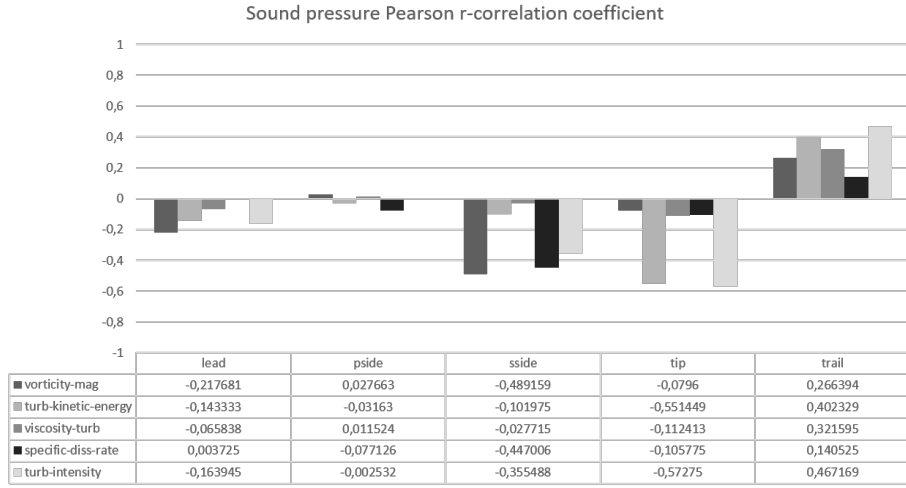


FIGURE 6.3: SPL to flowfield turbulence values correlation

6.3 Frequency analysis results

6.3.1 Results postprocessing

The time specific sound pressure values were further processed by a Python script presented in Appendix ???. As described in chapter 5, the timestep set in the CFD analysis was order of magnitude smaller than required by the direct method. The presented algorithm samples every 10th timestep to an intermittent tabular data frame and performs a Discrete Fourier Transform as per formula 3.7. This outputs a complex vector 3.12 of 5015 Fourier coefficients, for every data point on an analyzed surface. Due to

large number of figures, the scatter plots of the aforementioned values are provided in the Appendix ?? in figures ??, ?? and ??.

Obtaining amplitudes and phase shift of ordinary frequencies is rather straightforward. Formulas 3.14 & 3.15 are used element-wise on a complex vector of Fourier coefficients for each node of given control surface. Results are saved to csv files with $\text{Amp}_k(f_{bin})$ and $\theta_k(f_{bin})$ data respectively.

A method for graphical presentation of the FFT analysis results is proposed. At this stage, all nodes on a 3D control surface, having (x, y, z) coordinates are now linked to a 2D spectrum plot, therefore a dataset is now five dimensional, with one dimension being easily reduced. For first assessment of spectrum plots a "spectrum heatmap" is proposed. A heatmap kind plot with x-axis being the frequency bins, y-axis – the node number, and cell color is the magnitude of given frequency bin of given node. Exemplary heatmap is presented in fig. 6.4. Such approach provides some basic qualitative insight to the frequency distribution.

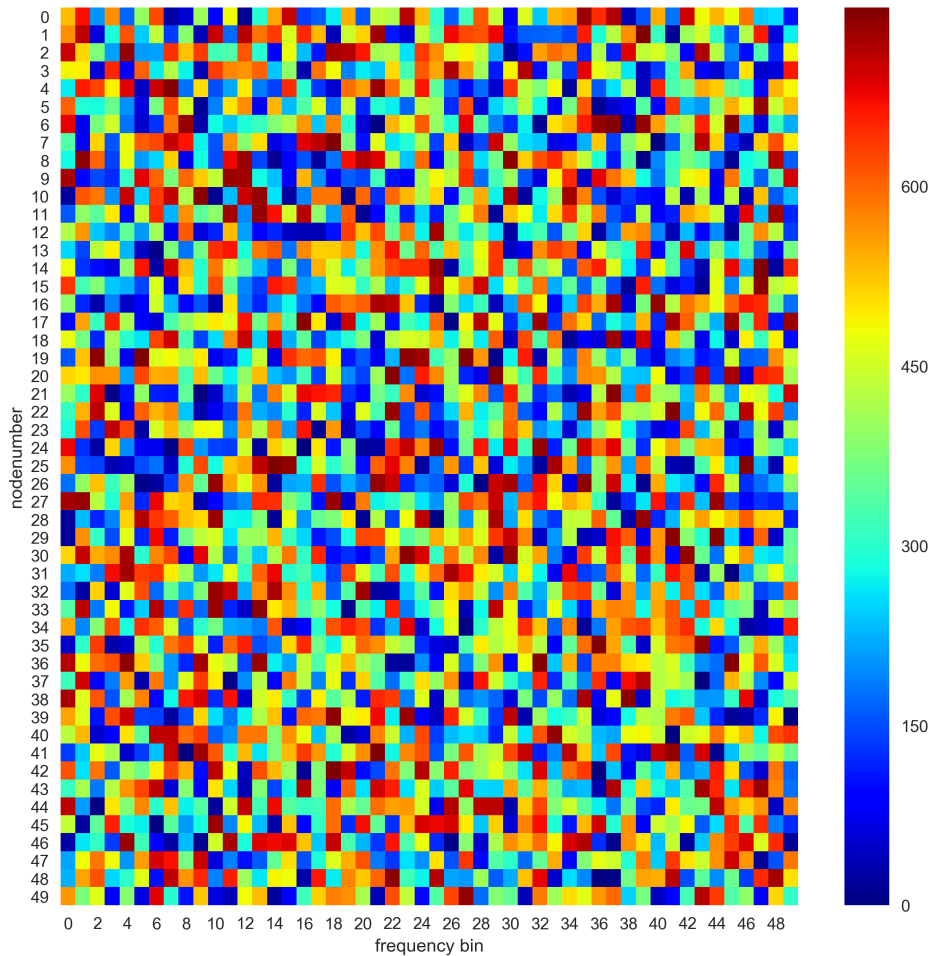


FIGURE 6.4: Exemplary FFT heatmap of magnitude. Random data.

Spectrum plot amplitude range as well as maximum FFT amplitude range are normalized and presented on a logarithmic scale as per formula 6.1.

$$\text{Amp}_{kn} = 20 \cdot \log_{10} \left(\frac{\text{Amp}_k}{\text{Amp}_{max}} \right) \quad (6.1)$$

where Amp_{max} is the global maximum amplitude of all datasets.

This operation has been performed separately on spectrum plots and peak amplitude plots. For spectrum plots the lower [dB] range is calculated by applying the formula 6.1 to global minimum and global maximum amplitudes, resulting in lower end of the scale of -226.41 dB, rounded down to -230dB. For surface plots, where only peak amplitudes are taken into account, the lower end of the plotting range is set as follows: obtain list of maximum amplitudes from all control surfaces, next take the minimum value from the obtained list and apply the aforementioned formula. The lower limit of the surface amplitude plots is calculated to -62.94 dB, rounded down to -65dB. This ensures that color range on is consistent throughout the spectrum plots and surface plots, with maximum value of 0 on every amplitude plot, corresponding to the maximum amplitude value.

Frequency of maximum amplitude for each node is obtained from the dataset. Moreover an amplitude weighted average frequency is calculated (eq. 6.2) to show the dominating frequency range on the given control surface. Frequency range presented on these plots is limited slightly above the maximum frequency possible to resolve by the presented approach and the limits are 0Hz and 25000Hz.

$$\bar{f} = \frac{\sum_{k=1}^N f_{bin_k} \cdot \text{Amp}_k}{\sum_{k=1}^N \text{Amp}_k} \quad (6.2)$$

6.3.2 Qualitative analysis

Analysis of the spectrum plots of the internal surfaces shows the following phenomena. At lower node numbers – towards the inlet of the domain, the lower frequencies are dominant in the spectrum, with little or no high frequency constituents. With increasing node numbers – moving towards the domain outlet, the amplitude of the low frequencies is increasing, whilst the high frequency constituents are also increasing their magnitudes. This pattern is repeated throughout the internal surfaces plots, including the tip internal surface. Moreover, the general observation is, that the magnitudes of given frequency bins, for corresponding node numbers, is increasing along with the distance from the hub. Therefore, the "quietest" region of the flowfield is upstream of the blade and near the hub and the "volume" of the sound increases towards the trailing-edge-to-tip-juncture. One of the most important conclusions appearing from the spectrum plots is, that the

flow nearfield sound, although having source in seemingly random flow fluctuations, is not random nor has a characteristic of white noise. The spectrum plots are lacking the information on the node locations, therefore spatial analysis of the plots poses some difficulties. Further analysis is done on internal surface and blade surface plots.

Amplitude weighted average frequency plots reduces the high dimensional FFT dataset to a plot feasible to show in a printed form. Frequency spectrum is averaged and constituents of high amplitude are highlighted on the plot. The averaged frequency is in higher range of c.a. 10kHz on the int-01 surface (Fig. ??) and up to 15-16kHz on the int-tip surface (Fig. ??). These frequencies are represented by a high pitched noise, characteristic to operating jet engines and being one of two main sources of noise of the engine. The plot is consistent with RMS sound pressure and sound intensity plots, suggesting, that the main contributor to the averaged RMS sound pressure is the high frequency noise.

Surface plots of frequencies of maximum FFT amplitude show, that the highest frequency oscillations occur in highly separated regions of the flow: in the wake behind the trailing edge of the blade and in the leading edge-hub juncture induced secondary flow. Surprisingly, the highest frequency fluctuations were captured in tip-to-trailing-edge juncture, which is the region where the largest RMS sound pressure values were noted.

6.3.3 Quantitative analysis

Morbi rutrum odio eget arcu adipiscing sodales. Aenean et purus a est pulvinar pellentesque. Cras in elit neque, quis varius elit. Phasellus fringilla, nibh eu tempus 1venenatis, dolor elit posuere quam, quis adipiscing urna leo nec orci. Sed nec nulla auctor odio aliquet consequat. Ut nec nulla in ante ullamcorper aliquam at sed dolor. Phasellus fermentum magna in augue gravida cursus. Cras sed pretium lorem. Pellentesque eget ornare odio. Proin accumsan, massa viverra cursus pharetra, ipsum nisi lobortis velit, a malesuada dolor lorem eu neque.

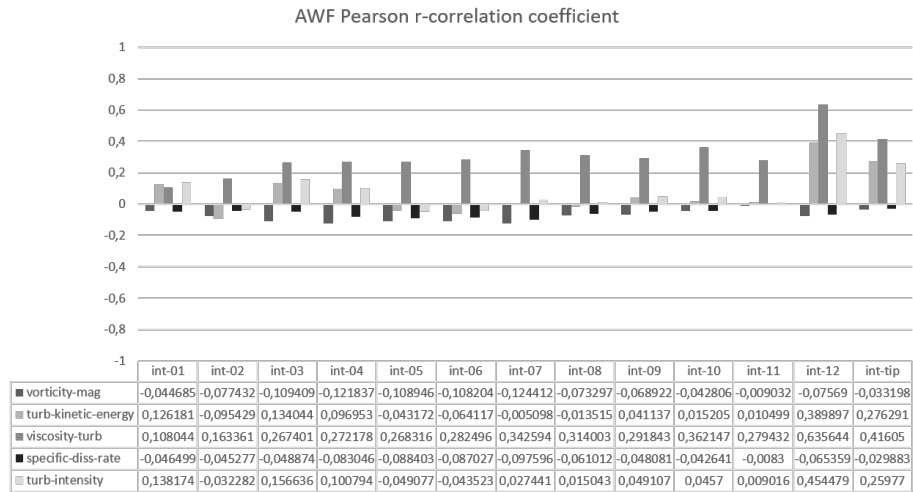


FIGURE 6.5: SPL to flowfield turbulence values correlation

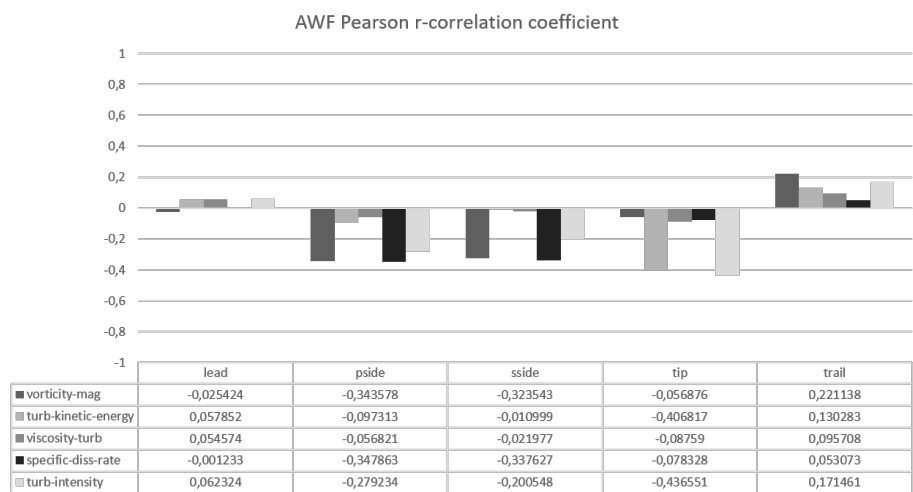


FIGURE 6.6: SPL to flowfield turbulence values correlation

Chapter 7

Conclusions & Further work

7.1 Results discussion

Initially, this thesis intended to investigate the following phenomena on a fan blade of a commercial large by-pass-ratio turbofan engine blade, yet no information on airfoil coordinates and efficiency figures of such devices are available for research purposes. It is assumed, that the phenomena that occur on such blade are similar in character to the ones obtained on the provided test case. Although the practical utilization of presented results is limited at this stage, some conclusion can be drawn out. The approach used on a NASA R67 transonic axial compressor provide some insight to noise generation phenomena in a "frozen-rotor" reference frame. It must be noted, that noise perceived by human or received by a microphone will be different from the ones presented. However, the noise perceived has it's source in the phenomena discussed in this thesis.

The main contributors to the blade's noise generation are the boundary layer separations induced by backflow in the boundary layer or by the shockwave boundary layer interaction. The existence of a shockwave in a device of that kind is also the main contributor of the so-called "buzzsaw noise", which may be recognized by simulating a rotor with a moving mesh and with a stationary receiver or data probe. Largest, in terms of amplitude and frequency, sound pressure fluctuations are found at the trailing edge of the blade and at trailing edge-tip junction. Sound pressure in decibel scale as well as average frequency per node of control surface are in expected range for this kind of device.

Following assumptions can be made. In order to reduce the noise generated by the transonic axial compressor blade one must eradicate the sources of separated flow and, if possible, provide a supersonic to subsonic transition of flow without inducing a shockwave. At time of preparation of this thesis, methods for inverse design of boundary shapes based on pressure and/or other design criteria exist in open source domain. Such software allows for generating airfoils for fixed wing aircraft and rotating machinery. Furthermore,

modification of shape of the blade trailing edge by implementing a shape that reduces the vortex shedding or at least the turbulence intensity in wake. At this stage, there are no suggestions for manipulating the frequency of the fluctuations.

Results of direct noise analysis on hub and casing surfaces are not presented due to a simple mistake – these surfaces were accidentally removed from the CFD solution export of the DDES analysis. Only one low frequency cycle is captured due to another mistake. As described in chapter 5, the timestep of the analysis was decreased by the order of magnitude in order to improve the analysis convergence. However, the solution export was still set up to deliver a dataset per timestep which resulted in a dataset 10 times larger than necessary, with no available walltime to continue the calculation.

The main downside of the presented study is lack of validation data for acoustical nearfield of the given case. It is assumed, that the approach is valid when two following factors coincide: if the CFD analysis that generate flow-field data is validated by experimental data and if FFT and RMS scripts return the expected results while the input is a sum of sine waves of known frequency, amplitudes and phase shifts. The CFD analysis results were validated with the experimental data provided in reference [27] as described in chapter 5, therefore it is assumed that the DDES flowfield data is valid. The RMS script return the expected average amplitude value while processing a set of sine wave signals, whereas the FFT script returned proper frequency spectrum and phase shift of the given signal. By this indirect validation, it is assumed that presented results are valid.

7.2 Improvements to the method

Current approach may be compared to attempts of resolving a turbulent boundary layer with one finite volume element at the boundary wall. Although mathematically possible (and used in wall modeled turbulence models) it is valid under fulfilling some assumptions. For presented direct approach, it is assumed that sinusoidal fluctuation of wavelength enclosed by four finite volumes and resolved by four timesteps.

Resolving a sinusoidal fluctuation with four finite volumes and four timesteps fulfills the continuity and momentum equations, any change in temperature, resulting in changing velocity of sound will disrupt the assumptions presented in chapter 3. FFT amplitude plots for ordinary frequencies, analyzed at random mesh points show, that the amplitudes of frequencies above the assumed by mesh and timestep range are dropped nearly to zero. A solution for this is using a finer mesh, capable of resolving shorter wavelength fluctuations, along with smaller timestepping to compensate for transition of sound wave in the finer mesh, especially in the boundary layer region and in the wake.

Considering that the mesh resolution is increased, a proper method for resolving turbulence flow is required. Although justified from the computational expense standpoint, the hybrid methods with shielding functions may result in filtering the source fluctuations at the boundary due to switching to the RANS part of given model. Using LES methods for further work will be considered.

Another aspect to be considered for improvement is the walltime management and data management. Presented analyses was performed on a Prometheus HPC and was distributed to 120 nodes. Normalized walltime for the analysis was above 1M CPU hours for both transition DDES and final DDES analyses and around 11TB of data was generated during the process. Using LES methods requires meshes of much greater density and therefore meshes of at least order of magnitude larger than used in this case. Assuming that walltime requirement is scaled linearly with the mesh size, assumed LES analysis of the presented test case, would have had required more than 10M CPU hours and around 1000CPU nodes.

Realtime processing of data to obtain sound information in the flowfield is impractical if even possible for full meshes, due to the amount of data generated. An efficient and high capacity storage storage is therefore required for performing direct approach analyses of sound on full flowfield.

Post-processing of data obtained in this study was performed with use of Matplotlib Pyplot library available for Python scripting language and hence the information about mesh was dropped during the process. This is visible especially in the internal surface scatter plots where lack of interpolation between points is visible. Using a post-processing tool with custom filters such as Paraview, or implementing a mesh file reader into Python (or any other implementation) scripts will solve problem with interpolation of data and allow visualization of full flowfield datasets.

7.3 Further work

As stated above, lack of validation case that directly checks the acoustical nearfield results is somewhat of a challenge. Therefore developing an experimental and numerical case of known acoustic nearfield properties is required.

The implementation of mesh reading or mapping to mesh functionality will be developed in further versions of the post-processing scripts. This will allow for more efficient qualitative an quantitative analysis of the obtained data.

Presented work describes a single passage of the compressor in stationary reference frame ("Frozen rotor") configuration and gives insight to basic aerodynamic phenomena contributing to noise. In order to asses the noise generation in compressor, or fan, flows

the analysis ought to be performed with use of rotating mesh with sliding interfaces and include effects of rotor-to-stator interaction, as well as interaction with compressor hub and casing. Furthermore, performing data acquisition and processing on full flow-field of the given case will give a better opportunity to post-process the obtained data. By extending the analysis time to more than 1 cycle of low frequency sound (0.05s), and preferably to more than five of such cycles, it may be possible to obtain information on acoustical wave modes within the flowfield of the case subject to study.

Considering that the geometry of given case is periodic, assuming the periodicity of flow in the DDES and LES analysis is prone to over constraining the resulting flowfield. Hence the analyses should be conducted on full rotor-stator stage, or at least a large portion of a stage, to eradicate or minimize the effect of periodic boundary conditions. This, combined with proposed LES simulation, enforces using a mesh with cell count in 10^8 order of magnitude, which leads to further challenges with data management and required computational resources.

7.4 Closing remarks

The study presented in this thesis can be interpreted two-wise. One as a case study on direct formulation of noise analysis and providing the minimum requirements towards the analysis. Second aspect is the study of generating sound by the transonic axial compressor rotor blade. Both aspects of the study are, at least partially, fulfilled.

The provided minimum requirements of the analysis proved to work at relatively high computational expense. Yet, using the acoustical analogies implemented into used CFD code with transonic flows with shockwaves is unjustified by the mathematical formulation of the FW-H analogy. The resolution of the obtained acoustical nearfield can be improved at a cost of higher computational power requirements.

The presented results of the compressors acoustical nearfield are rather expected and are relateable to relative mach number fields and time averaged static pressure fields. Results identify the sources of aerodynamic noise that are consistent with ones described in literature, turbulent regions of the flow are the source of pressure fluctuations of high amplitude and high frequency. Propagation of sound waves was captured for lower end of the frequency spectrum, while the effect of high pitch noise is captured as an increase in RMS sound pressure and decibel figures. These results can be used to design a compressor blade that generates lower aerodynamically induced noise.

The method will be improved in terms of efficiency and data storage and attempted to be used in other technical entities where noise generation and acoustical wave mode assessment is required.

Bibliography

- [1] International standards and recommended practices. annex 16 to the convention on international civil aviation. environmental protection. volume i. aircraft noise. Technical report, ICAO, 2011.
- [2] 7-year ifr flight movements and service units forecast: 2013-2019, 2012.
- [3] Challenges of growth 2013 task 4: European air traffic in 2035, 2013.
- [4] *ANSYS Documentation. Fluent Theory Guide*, 2015.
- [5] *Prometheus HPC maunual*, 2018. <https://kdm.cyfronet.pl/portal/Prometheus>.
- [6] J. D. Anderson. *Computational Fluid Dynamics*. McGraw-Hill, Inc., 1995.
- [7] A. Bjork and G. Dahlquist. *Numerical Methods*. Prentice-Hall, 1974.
- [8] R. Bracewell. *The Fourier Transform and Its Applications*. McGraw-Hill, Inc., 1965.
- [9] K. S. Brentner and F. Farassat. An analytical comparison of the acoustic analogy and kirchhoff formulations for moving surfaces. *AIAA Journal*, 36(8):1379–1386, 1998.
- [10] C. Choi and P. Moin. Grid-point requirements for large eddy simulation: Chapman’s estimates revisited. *Physics of Fluids*, 24(1), January 2012. <https://aip.scitation.org/doi/full/10.1063/1.3676783>.
- [11] J. E. Crouse, J. S. David, C. Janetzke, and R. E. Schwirian. A computer program for composing blading from simulated circular-arc elements on conical surfaces. Technical Report TN D-5437, NASA Langley Research Center, 1969.
- [12] W. S. Cunnan, W. Stevans, and D. C. Urasek. Design and performance of a 427-meter-per-second-tip-speed two stage fan having a 2.40 pressure ratio. Technical Report TP-1314, NASA Langley Research Center, 1978.

- [13] N. Curle. The influence of solid boundaries upon aerodynamic sound. *Proceedings of the Royal Society. Series A, Mathematical, Physical and Engineering Sciences*, 231(1187):505–514, September 1955. <http://rspa.royalsocietypublishing.org/content/231/1187/505>.
- [14] J. D. Durrant and J. H. Lovrinic. *Bases of Hearing Sciences. Second Edition*. Lippincott Williams and Wilkins, 1984.
- [15] J. O. Hinze. *Turbulence*. McGraw-Hill Publishing Co., 1975.
- [16] D. L. Huff. Noise reduction technologies for turbofan engines. Technical Report NASA/TM—2007-214495, NASA Glenn Research Center, 2007.
- [17] R. King. Part ii: Turbomachinery. In *Active Flow Control II*, pages 134–210, 2010.
- [18] J. B. Lee, D. Edmonds, and D. Rhodes. Ercd report 1101. noise exposure contours for heathrow airport 2010. Technical report, CAA, 2011.
- [19] M. J. Lighthill. On sound generated aerodynamically i. general theory. *Proceedings of the Royal Society. Series A, Mathematical, Physical and Engineering Sciences*, 211(1107):564–587, March 1952. <http://rspa.royalsocietypublishing.org/content/211/1107/564>.
- [20] M. J. Lighthill. On sound generated aerodynamically ii. turbulence as a source of sound. *Proceedings of the Royal Society. Series A, Mathematical, Physical and Engineering Sciences*, 222(1148):1–32, March 1954. <http://rspa.royalsocietypublishing.org/content/222/1148/1>.
- [21] J. Mosiezny. Github repository for nasa r67 input data and noise analysis, 2018. <https://github.com/JedrzejMosiezny/R67-data-analysis>.
- [22] T. Oetkier, H. Partl, I. Hyba, and E. Schleg. *The Not So Short Introduction to LATEX 2e*, 2018. <https://tobi.oetiker.ch/lshort/lshort.pdf>.
- [23] A. Schwarz and J. Janicka. *Combustion Noise*. Springer Science and Business Media, 2009.
- [24] J. Smagorinsky. General circulation experiments with the primitive equations. *Monthly Weather Review*, 91(3):99–164, 1963.
- [25] P. R. Spalart et al. A new version of detached-eddy simulation, resistant to ambiguous grid densities. *Theoretical and Computational Fluid Dynamics*, 20:181–195, 2006.

- [26] P. R. Spalart, W. H. Jou, M. Strelets, and S. R. Allmaras. Comments of feasibility of les for wings, and on a hybrid rans/les approach. In *First International conference: Advances in DNS LES: Direct numerical simulation and large eddy simulation*, pages 137–148, 1997.
- [27] A. J. Strazisar, J. R. Wood, M. D. Hathaway, and K. L. Suder. Laser anemometer measurements in a transonic axial-flow fan rotor. Technical Report TP-2897, NASA Langley Research Center, 1989.
- [28] P. Traub. Noise aspects of future jet engines. Technical report, LTH Triebwerke, 2012.
- [29] D. C. Urasek, W. T. Gorrel, and W. S. Cunnan. Performance of a two-stage fan having a low-aspect-ratio, first-stage rotor blading. Technical Report TP-1493, NASA Langley Research Center, 1979.
- [30] H. K. Versteeg and W. Malalasekera. *An introduction to Computational Fluid Dynamics: The Finite Volume Method*. Longman Scientific & Technical, 1995.
- [31] C. Wagner, T. Hüttl, and P. Sagaut. *Large-Eddy Simulation for Acoustics*. Cambridge University Press, 2007.
- [32] I. Wieczorek and J. Mosieżny. Development of air transport in statistical terms. *Journal of Mechanical and Transport Engineering*, 66(1):51–68, 2013.
- [33] J. E. F. Williams and D. L. Hawkings. Sound generation by turbulence and surfaces in arbitrary motion. *Philosophical Transactions of the Royal Society of London. Series A, Mathematical and Physical Sciences*, 264(1151):321–342, May 1969. <http://www.jstor.org/stable/73790>.